Soil Dynamics and Earthquake Engineering 182 (2024) 108740

Contents lists available at ScienceDirect

Soil Dynamics and Earthquake Engineering

journal homepage: www.elsevier.com/locate/soildyn

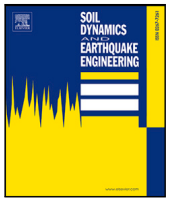

Dynamic impedance and compliance surfaces of twin adjacent surface foundations under synchronous and asynchronous loads

Hendrawan D.B. Aji [a,*], Till Heiland [b], Frank Wuttke [a], Alexander Stark [b], Petia Dineva [c]

[a] Institute of Geosciences, Chair of Geomechanics and Geotechnics, Kiel University, Kiel, Germany
[b] Institute of Concrete Structures and Building Materials, Concrete Section (IMB), Karlsruhe Institute of Technology (KIT), Karlsruhe, Germany
[c] Institute of Mechanics, Bulgarian Academy of Sciences, Sofia, Bulgaria

ARTICLE INFO

Dataset link: https://doi.org/10.57892/100-50

Keywords:
3D dynamic soil–structure interaction
Hybrid BEM-FEM
Two adjacent foundations
Impedance/compliance function
Asynchronous harmonic loads
Phase shift
Frame bridges
Commercial program ABAQUS

ABSTRACT

The 3D dynamic response of twin rigid massless foundations under concurrent time-harmonic loads in a finite soil region resting on a homogeneous visco-elastic half-space is studied. The mechanical model is based on an efficient approach combining the boundary element method (BEM) for the semi-infinite far-field zone and the finite element method (FEM) for the finite near-field geological region. The accuracy and convergence study of the hybrid computational scheme based on the macro-element concept is presented. A parametric study revealing the sensitivity of the dynamic response to the following key model parameters: *(1)* Poisson's ratio of the semi-infinite zone; *(2)* separation distance between foundations; *(3)* material damping; *(4)* the foundations' geometry; and *(5)* the phase shift between the acting harmonic loads is presented. The obtained results show resonance patterns as a result of the mutual play between foundations' geometry, their spatial arrangement, and soil properties. Approximation formulae are proposed to estimate the resonance states. The results also show that the effect of material damping cannot be fully decoupled from the impedance functions using the conventional formula. Further, the presence of a phase between harmonic loads acting on the foundations influences the resonance state, and negligence of it may lead to unexpected responses of the foundations. An efficient optimization of the dynamic design of structures with adjacent foundations, such as bridges, offshore and onshore infrastructures with multiple foundations, machinery, or adjacent structures, could be performed using the obtained results. For better accessibility, the solutions are presented in the form of 3D impedance and compliance surfaces, and they are readily downloadable as interactive figures. A calculation example is given in the appendix.

1. Introduction

The term foundation–soil–foundation interaction (FSFI) reflects the collective interaction between multiple vibrating foundations and the soil domain. The understanding of FSFI is important for structures with closely spaced foundations such as bridges, offshore and onshore structures with multiple foundations, machinery, etc., or closely adjacent structures. A group of foundations involves both the modification of the ground motion and the alteration of the dynamic response of each foundation, due to multiple interactions that occur as the foundations are rested or inserted in the geological continuum. Such a complex interaction includes the following key factors: (1) the stiffness contrast between the foundations and the soil, (2) the spatial discontinuities along their interfaces, (3) the spatial arrangement of the foundations/structures, (4) the eigenfrequencies and eigenmodes of the soil–foundation–structure systems, (5) the excitation's or ground motion's characteristic and actively propagating waves, (6) the site effect due to impedance contrasts of soil layers, and (7) the effects of nonlinearities, in the case of strong vibrations. With respect to the problem's geometrical representation, the complexity of soil–structure interaction (SSI) problems can be approached numerically using either *(a)* the direct or single-step method, where the structure of interest and its near-field region is modeled and the whole domain is solved in one step, or *(b)* the substructure or multistep method [1–3]. In the latter method, the problem is decoupled into *(b1)* a kinematic interaction analysis involving the soil and massless foundations/structures, from which the result is foundation's input motion (FIM) or impedance functions; and *(b2)* an inertial interaction analysis, in which the obtained FIM or impedances are coupled with the foundation-structure system (and its mass) to obtain its inertial response. For foundations

* Corresponding author.
E-mail addresses: hendrawan.aji@ifg.uni-kiel.de (H.D.B. Aji), till.heiland@kit.edu (T. Heiland), frank.wuttke@ifg.uni-kiel.de (F. Wuttke), alexander.stark@kit.edu (A. Stark), petia@imbm.bas.bg (P. Dineva).

https://doi.org/10.1016/j.soildyn.2024.108740
Received 7 March 2024; Received in revised form 3 May 2024; Accepted 21 May 2024
Available online 31 May 2024

or structures with relatively simple configurations and elastic material behavior, the substructure method is preferable due to its lower computational demand. In addition, kinematic interaction analyses, such as described in *(b1)*, facilitate a thorough understanding of the governing mechanism of the problem and the role of key parameters. What follows is a short evaluation of the state of the art regarding available mechanical models concerning the dynamic behavior of a system of soil and adjacent spread foundations.

The importance of the FSFI phenomenon in dynamic and seismic structural design and analysis has long attracted the attention of the scientific community. Savidis and Richter [4] employed an analytical formulation to examine the FSFI problem, in which Holzöhner influence functions for constant stress distribution over rectangular regions were used. Two rigid massless rectangular foundations on the surface of a linear-elastic, isotropic half-space were the object of interest. Later, the method was used to extend the study considering linear visco-elastic half-space by Gaul [5]. In both cases, relaxed boundary conditions in the contact between the soil and foundations were considered. Triantafyllidis and Prange [6] improved the assumption by considering non-relaxed (complete bond) boundary conditions in their study, in which they used a set of Fredholm's integral equations of the first kind and solved them using the Bubnov–Galerkin method. They discussed an intriguing case study of the dynamic interaction of railway sleepers. Liou [7] proposed to solve the problem by decomposing arbitrarily prescribed stress boundary conditions on the surface of a half-space to obtain analytical solutions of the 3D wave equation. The solution for two foundations was subsequently obtained by the superposition of interaction stresses. Aldaikh et al. [8] proposed an analytical solution for the static stiffness coefficients of adjacent foundations and suggested that the results have good agreement with the experimental ones.

A numerical study on this topic using the finite element method (FEM) can be found in Kausel et al. [9]. Gonzales [10] utilized the FEM in conjunction with the consistent boundary method to study the interaction between two square rigid massless spread foundations. Further research using this approach can be found in Lin et al. [11], among others.

Wong and Luco [12] approached the dynamic interaction problem of two rigid square foundations resting on a visco-elastic half-space using the discretized boundary integral equation technique, supplemented with an iterative scheme to improve its solution. Numerical studies on the topic using the boundary element method (BEM) were performed by Qian and Beskos [13,14], in which the response of two square massless foundations subjected to external load or seismic waves was of interest. This study was later extended for flexible surface foundations of arbitrary shape using the BEM-FEM in Qian et al. [15]. Additionally, Betti [16] used the BEM in conjunction with the substructure deletion method to obtain the FIM. Karabalis and Mohammadi [17] used the 3D BEM in the frequency domain to examine the compliance functions of two and three adjacent foundations. Sbartai [18] later extended this study by a deeper examination of each parameter's influence and for more vibration modes using the BEM and the thin-layer method [19,20]. Aji et al. [21] studied the influence of adjacent foundations on surface wave fields caused by a buried dynamic source using the BEM-FEM, taking into account the damaged states of the materials. Zeolla et al. [22] investigated the group effect of twin foundations under simultaneous loads using the finite difference method (FDM), enhanced with viscous dampers, and proposed impedance modifiers to account for the group effect.

The influence of SSI on typical railroad frame bridges was thoroughly examined by Heiland et al. [23] through multiple numerical approaches: (1) the FEM in conjunction with tuned dampers and (2) the hybrid BEM-FEM. One of the key findings was that the soil-bridge system experiences a change of state depending on the ratio between the first bending mode of its frame, f_1, and the frequency of the vertical rigid body mode of its soil–foundation systems, f_B, i.e., $\eta = f_1/f_B$. At $0 \leq \eta < 1$, the soil-bridge system responds vertically in phase to a vertical harmonic load, similar to a single-degree-of-freedom (SDOF) system, and the radiation damping tends to increase with the abutment's stiffness. The soil-bridge system conversely responds as a multi-degrees-of-freedom (MDOF) system at $\eta > 1$, at which the soil–abutment system and the bridge's frame move asynchronously relative to each other. The damping in this state decreases as the abutment's stiffness increases. Such a phenomenon highlights the importance of FSFI in practical engineering cases and raises the question of integrating the FSFI effects into the practical modeling procedure. For the practical modeling of portal frame bridges, Heiland [24] proposed a conservative estimation of the frequency range influenced by FSFI and derives application limits for quasi-static SSI approaches. The aim is to minimize the influence of FSFI on the overall dynamic system. Another example is the dynamic design of offshore wind turbine's support structure, in which the structure's natural frequencies must not interact with the rotor's and blade passing frequencies, e.g., in [25]. Such a support structure can be founded on a multi-contact foundation, e.g., a tripod or a jacket. This means that the identification or estimation of the natural frequencies of such a system, including the FSFI effect, under synchronous and asynchronous harmonic loads is crucial in its design.

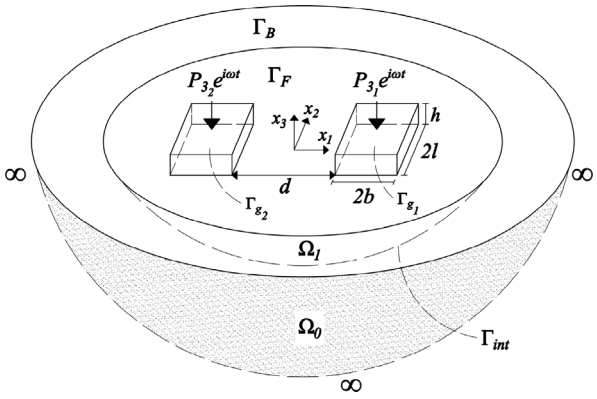

Fig. 1. Problem geometry presenting the general configuration of two surface foundations resting on a finite region Ω_1, which is embedded in a half-space Ω_0.

Most of the aforementioned studies regarding the foundations' response to externally applied loads considered a condition, in which the harmonic load is applied to one foundation. Meanwhile, the behavior of such a system's kinematics under concurrent harmonic loads is not yet well understood. Note that for cases in which both kinematic and inertial interactions in a group of structures are directly taken into account, discussions can be found under the topic structure–soil–structure interaction (SSSI) or site-city interaction, e.g., in [24,26–31], among others, while studies investigating the influence of asynchronous FIMs on a structure's response can be found in [32,33], among others. For a deeper understanding of the dynamic behavior of foundation–soil–foundation systems under synchronous and asynchronous vertical harmonic loads, we perform here an extensive numerical study on the dynamic response of twin rigid massless surface foundations subjected to concurrent time-harmonic loads. The study is focused on the kinematic interaction between the foundations and soil, and the results are presented in the form of dynamic impedances and compliances. The choice of limiting the study to surface foundations and a homogeneous visco-elastic half-space is taken because the aim is to better understand the governing kinematics of the system. The study is performed using the hybrid BEM-FEM implemented in ABAQUS and MATLAB, which is capable of handling problems involving arbitrary layered half-space [30].

The paper is organized as follows. The mathematical description of the problem is presented in Section 2, while the accuracy and the convergence study of the proposed hybrid numerical scheme is given in Section 3. The parametric study setup and results are discussed in Section 4. The computational aspect of the numerical study is illustrated in Section 5, followed by the conclusions in Section 6.

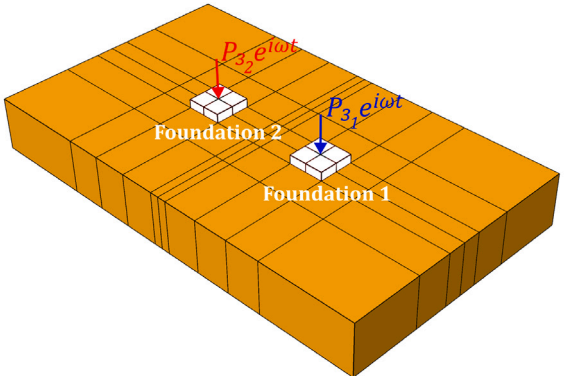

(a) FE model of two foundations under harmonic loads and resting on a finite soil region.

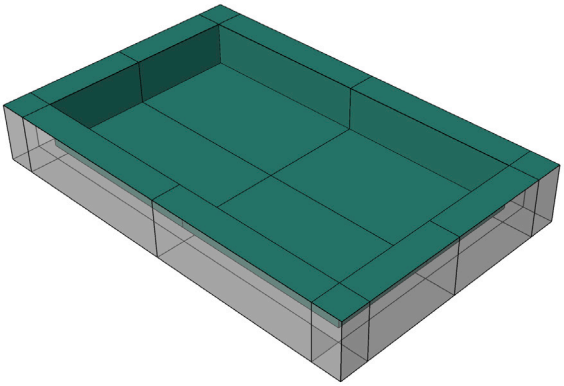

(b) BE model. Active elements are in green, and dummy elements are transparent.

Fig. 2. Example of a couple FE and BE digital models.

2. Problem description

An idealization of the problem is given in Fig. 1. Two foundations rest on a finite soil region, which is embedded in a homogeneous visco-elastic half-space. The foundations and the supporting near-field soil region are modeled using finite elements (FEs), whereas the half-space is computed using boundary elements (BEs). The half-space is marked as Ω_0, and the finite soil region is denoted as Ω_1. The interface between BE and FE subdomains is denoted as Γ_{int}. The traction-free surfaces of the FE and BE regions are denoted as Γ_F and Γ_B, respectively, such that $\Gamma_{\Omega_1} = \Gamma_{int} \cup \Gamma_F \cup \Gamma_{g_j}$ and $\Gamma_{\Omega_0} = \Gamma_{int} \cup \Gamma_B$. Here, $\Gamma_{g_j}, j = 1, 2$, are the interfaces between foundations and the finite soil region. Note that Γ_{int} can take an arbitrary shape. Examples of the FE and BE numerical models are shown in Fig. 2.

The foundations are congruent with a length of $2l$ and a width of $2b$, and they are separated by an edge-to-edge distance d. The foundations are assumed to be massless and rigid, therefore, their height, h, and material properties do not play any role.

The material properties of Ω_0 and Ω_1 are the same: shear wave velocity $C_S = 1$ m s^{-1}, density $\rho = 1$ kg m^{-3}, shear modulus $\mu = 1$ Pa. The Poisson's ratio is either $\nu = 1/3, 0.40$, or 0.49. A material (hysteretic/viscous) damping, β, of either 0%, 5%, or 10% is considered. The shear modulus is modified by the damping such that $\mu^* = \mu(1+2i\beta)$, where $i = \sqrt{-1}$. Thus, the corresponding shear wave velocity in this case is $C_S^* = \sqrt{\mu^*/\rho}$.

The following boundary conditions are taken into account: (1) Sommerfeld's radiation condition at infinity is satisfied in the semi-infinite region, Ω_0; (2) along the free-surfaces, Γ_F and Γ_B, the tractions $t_j = \sigma_{jk} n_k, j = 1, 2, 3; k = 1, 2, 3$, are zero, where σ_{jk} is the stress tensor and n_k is the outward normal of respective surfaces; (3) along the interface, Γ_{int}, compatibility and dynamic equilibrium conditions of displacement, u_j, and traction, t_j, are enforced ($j = 1, 2, 3$); (4) likewise, non-relaxed (complete bond) boundary conditions are applied on the contact between foundations and the soil (Γ_{g_j}) except the contact in models used for the convergence study. The definition of these boundary conditions can be found in [34]. The assumption of a non-relaxed contact is closer to reality since spread foundations are usually built *in situ*, on top of a lean concrete layer. In addition, the soil region and half-space are assumed to remain in an elastic state, i.e., low-strain vibration, see [23,35].

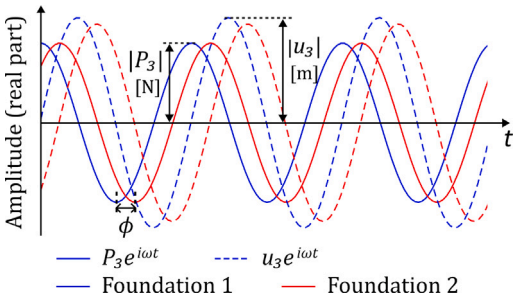

Fig. 3. Illustration of asynchronous vertical harmonic loads applied on two foundations, $P_{3_j} e^{i\omega t}$, and its displacement responses, $u_{3_j} e^{i\omega t}, j = 1, 2$. The phase shift between the harmonic loads, ϕ, here is 45°. The amplitudes are $P_{3_1} = P_3$, i.e., it only has a real component, and $P_{3_2} = P_3(\cos\phi - i \sin\phi)$. Both have the same magnitudes, $|P_3|$.

The harmonic loads, $P_j e^{i\omega t}$, are applied to the center-top of both foundations (Figs. 1 and 2(a)), while the foundations' response is measured at their center-bottom nodes. The foundation's response is presented in the form of an impedance and a compliance which are described as

$$S_{jk}(\omega) = \frac{P_j e^{i\omega t}}{u_k e^{i\omega t}} \quad \text{and} \tag{1}$$

$$V_{jk}(\omega) = \frac{u_k e^{i\omega t} \mu b}{P_j e^{i\omega t}}, \tag{2}$$

respectively. Here, $P_j, j = 1, 2, 3$, are the complex-valued amplitude of the load (N), ω is the angular frequency (rad/s) and the scalar t denotes time (s). A phase shift in the periodic load, ϕ, can be inserted through modification of the complex-valued amplitude, P_j, i.e., $P_j e^{i(\omega t - \phi)} = \left(P_j(\cos\phi - i \sin\phi)\right) e^{i\omega t}$. Inversely, ϕ between two harmonic loads can be computed by taking the real part of the ratio between the amplitudes, P_{j_1} and P_{j_2}, as follows:

$$\phi = \arccos\left(\Re\left(\frac{P_{j_2}}{P_{j_1}}\right)\right). \tag{3}$$

An illustration of asynchronous harmonic load time functions is given in Fig. 3, where $\phi = 45°$.

We present the impedance and compliance results as 2D functions and 3D surfaces. The more general form of impedance functions is more convenient and accessible to use in dynamic-resistant designs. Computed impedances can be coupled to a model of foundation or structure to obtain a complete, i.e., kinematic and inertial, dynamic response of a soil–structure system (see [36,37]; Appendix). Alternatively, one can use the frequency-dependent impedances in a time-domain analysis, e.g., by using the time-domain transformation method [38], among others. Thus, from a practical point of view, practicing engineers may find them more useful. On the other hand, compliance functions are better for identifying a trend in the response, such as resonance patterns of a soil–foundation system. We also present the impedance and compliance surfaces as interactive figures to improve their practical usefulness (https://doi.org/10.57892/100-50).

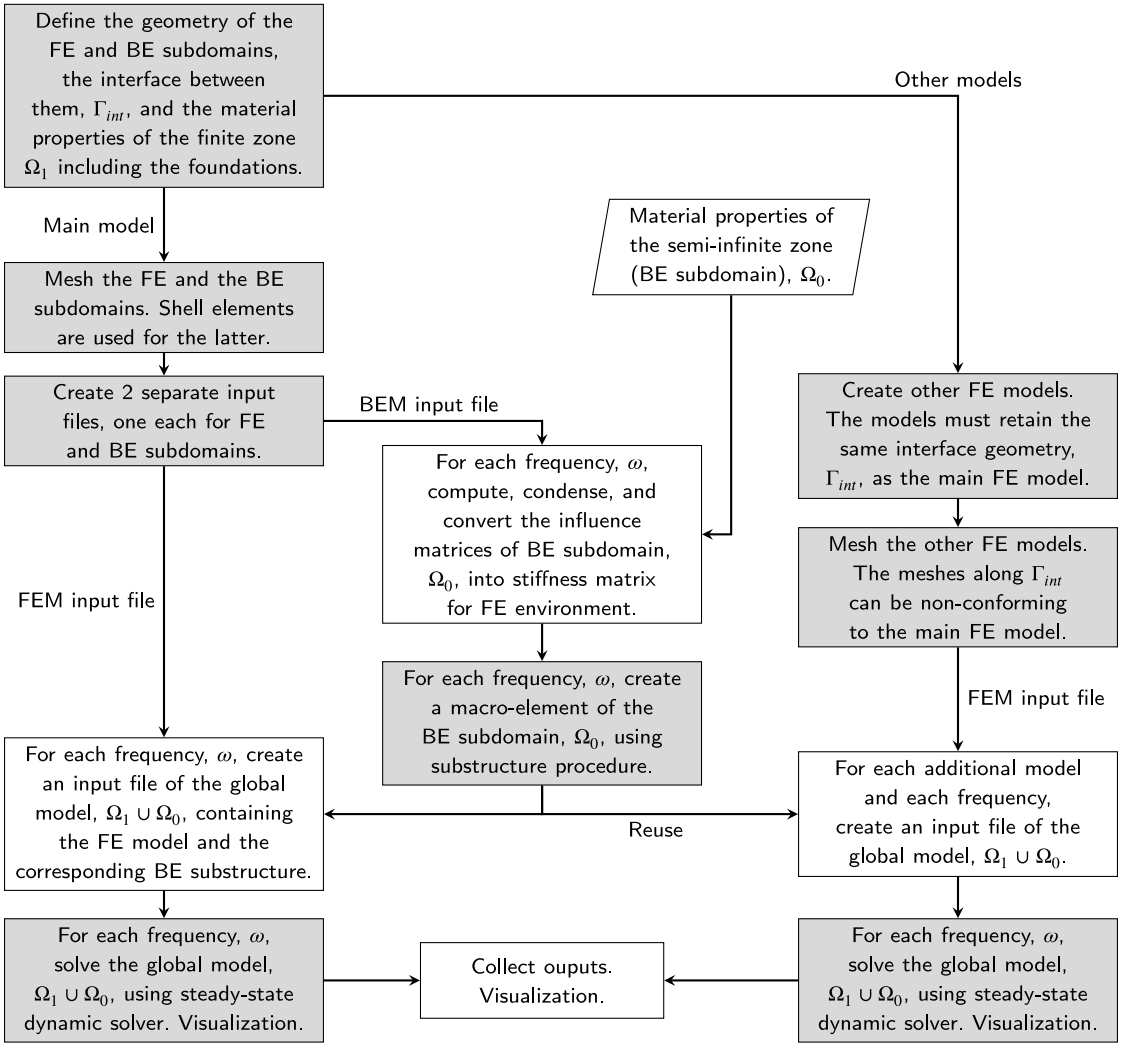

Fig. 4. Flowchart of the hybrid BE-FE method based on the extended macro-element concept. The gray color marks processes performed in the ABAQUS environment, while the white marks those performed in MATLAB.

The complex-valued impedance is decoupled into its real and imaginary parts as [37]

$$S_{jk}(\omega) = K_{jk}k_{jk}(\omega) + i\omega C_{jk}c_{jk}(\omega), \tag{4}$$

where K_{jk} and C_{jk} are the static terms. The multipliers $k_{jk}(\omega)$ and $c_{jk}(\omega)$ are the corresponding frequency-dependent coefficients, which can be derived as

$$k_{jk}(\omega) = \frac{\Re\left(S_{jk}(\omega)\right)}{K_{jk}} \quad \text{and} \tag{5}$$

$$c_{jk}(\omega) = \frac{\Im\left(S_{jk}(\omega)\right)}{\omega C_{jk}}, \tag{6}$$

respectively. By substituting and rearranging Eqs. (5) and (6) into the fundamental equations of linear dynamics with respect to the hysteric damping of soils (omitted for brevity), the radiation damping β_R is obtained. This involves determining the ratio between the imaginary ($\Im$) and real ($\Re$) components of the impedance function:

$$\beta_R = \frac{\Im\left(S_{jk}(\omega)\right)}{2 \cdot \Re\left(S_{jk}(\omega)\right)} \tag{7}$$

We avoid addressing the real and imaginary parts as the dynamic stiffness and radiation damping since this may mislead engineers. The real and imaginary parts (or the in-phase and out-of-phase parts) of impedances should be understood as a pair of data, which describes the magnitude and the phase of a system in response to a harmonic load. This means that these values can be negative, which merely describes the response's phase shift.

We find that we can present the imaginary (or out-of-phase) coefficients for some cases better using the term $a_0 c_{jk}(\omega)$, with the use of which the high values in the near-static region can be avoided. For these cases, the impedance can be computed as

$$S_{jk}(\omega) = K_{jk}k_{jk}(\omega) + iC_{jk}\frac{C_S}{b}a_0 c_{jk}(\omega), \tag{8}$$

where a_0 is the normalized frequency, i.e., $a_0 = \omega b C_S^{-1}$. We limit our present study to vertical–vertical impedance coefficients or compliances as functions of the normalized frequency, i.e., $k_{33}(a_0)$ and $c_{33}(a_0)$ or $V_{33}(a_0)$. Here, we use the static terms defined in [37] as follows:

$$K_{33} = \left[\frac{2\mu l}{(1-\nu)}\right]\left(0.73 + 1.54\chi^{0.75}\right); \tag{9}$$

$$C_{33} = \rho C_L A_b, \text{ where} \tag{10}$$

$$\chi = \frac{A_b}{4l^2}; \quad C_L = \frac{3.4C_S}{\pi(1-\nu)}. \tag{11}$$

The term C_L refers to Lysmer's analogue wave velocity and A_b denotes the area of a foundation, i.e., $A_b = 2l \times 2b$ for a rectangular foundation.

Numerical solution

The mechanical problem is solved using the hybrid BE-FE method implemented in ABAQUS and MATLAB [21,30,39]. The BEM here handles the semi-infinite region. The FEM is utilized to compute the near-field region and solve the global system of equations (SEs) in the frequency domain. The coupling method is an extension of the direct, FEM-hosted approach developed by Vasilev et al. [40]. The standard collocation technique is used in the BEM implemented here. The BEM influence matrices for the far-field region are computed for each frequency, ω, and then condensed and converted into a suitable form for the FE environment. The converted matrices are then generated into macro-elements using the substructure procedure in ABAQUS and subsequently attached to the computed SEs of the FE subdomain, resulting in the global SEs. Finally, the latter is solved using a direct-solution steady-state dynamic solver in ABAQUS. The workflow is illustrated in Fig. 4. The verification of the coupling method is presented elsewhere for the following cases: (1) the dynamic response of a rigid massless foundation resting on a half-space in [21]; (2) the dynamic response of a rigid massless foundation on the surface of an arbitrary layered half-space in [30]; (3) wave propagation due to incident waves in [21]; (4) wave propagation through a layered soil due to a double-couple point source in [39]. The details of the coupling method are also available in the aforementioned sources and are not repeated here for the sake of brevity.

The advantages of the current method include the followings: (1) dynamic soil–structure problems involving complex structural models can be considered due to the extensive element library of the FEM; (2) Sommerfeld's radiation condition at infinity is satisfied and the model domain can be minimized, reducing computational cost; (3) different types of dynamic or seismic source can be considered (see [39]); (4) multi-layer problems with an arbitrary number of layers and geometry can be considered, while avoiding high computational memory cost (see [30]); (5) non-conforming BE and FE meshes along the interface can be used, providing modeling flexibility; and (6) the macro-elements of the BE subdomain can be transferred and reused for other FE models (see [39]). The computation benefit for the current study is quantified in Section 5.

The frequency domain BEM-FEM employed here results in complex-valued outputs, i.e., pairs of real and imaginary data. Some results in the following sections are presented in the form of a value at a phase angle relative to its corresponding real value. In these cases, the phase of the output is denoted as $\bar{\phi}$. For example, plotting the displacement at $\bar{\phi} = 0°$ and $-90°$ results in the real and the imaginary part of displacement, respectively.

The FEM leads to sparse symmetric positive definite matrices, while the BEM based on the collocation technique leads to fully non-symmetric ones. As a result, the global matrices in our proposed direct hybrid method are large, only partially sparse, and non-symmetric. To solve this, one can utilize ABAQUS's unsymmetric matrix storage and solver, see [41]. The disadvantage of the direct coupling method relative to the iterative method in terms of matrix storage and solver is compensated by the omission of necessary iterations. In addition, our improvement in allowing the reuse of the macro-elements further extends the advantage of the direct method by reducing computation time, as illustrated in Section 5.

Limitations of the study

The current study considers a linear visco-elastic homogeneous half-space supporting the foundations. In addition, the soil here is assumed to be in a dry condition. Although such a soil condition with constant material properties is uncommon in nature, the results presented here offer an understanding of the governing interaction between the surface foundations and soil in the case of synchronous and asynchronous loads, which is important for understanding more complex problems.

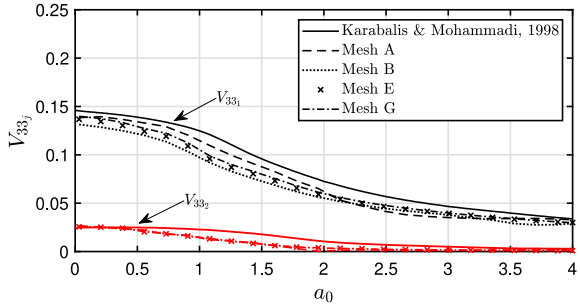

(a) Compliance function V_{33} vs. a_0.

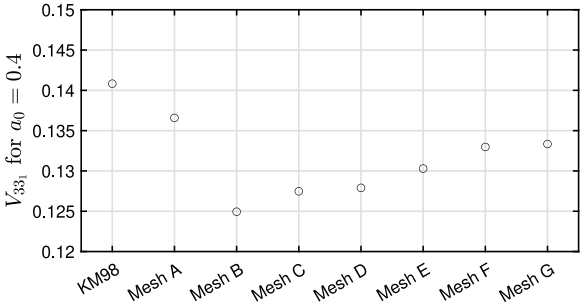

(b) Influence of mesh sizes on the result for $a_0 = 4$.

Fig. 5. Comparison of vertical compliance functions obtained from models with one load-sustaining foundation for varying mesh setup and with existing solution.

On the other hand, previous studies showed that the impedances of a foundation embedded in a thick topsoil may be very well approximated by those of a foundation embedded in a half-space, e.g., $h_s/r > 20$ in the case of the horizontal impedance of a foundation embedded in a poroelastic soil [42] and $h_s/b > 12$ in the case of the vertical compliance of foundations resting on a soil overlaying a bedrock [18]. Here, h_s is the topsoil thickness and r is the foundation's radius. In addition, the assumption of a linear elastic material behavior taken here is only suitable for problems involving low-strain vibrations (see [35]), such as those associated with traffic or machine operations [23]. Consequently, the effects of nonlinear material and contact behaviors such as liquefaction, sliding, uplifting, or gapping are not within the scope of this study. We also only consider vertical harmonic loads to adhere to the space limit. Broader analyses and discussions on topics covering the effects of foundation embedment, layered soil, groundwater table/saturation, and an additional number of foundations are reserved for future studies. In a broader sense, the authors' idea is to develop in the near future a library of BEM models, modeling the semi-infinite domain with complex properties such as material anisotropy, poroelasticity, physical and geometrical nonlinearity, and material gradient and heterogeneity of different types. All these models are based on different analytically derived fundamental solutions or half-space Green's functions, which are themselves complex tasks of mathematical physics.

3. Mesh convergence and setup

To study the mesh convergence, a case of two adjacent rigid foundations, where only one of them is subjected to a vertical harmonic load, is taken into account. The problem's solution was given by Karabalis and Mohammadi [17] using the BEM in the frequency domain. The results are presented in the form of $V_{33_j}, j = 1, 2$, where the subscript $j = 1$ refers to the load-sustaining foundation and $j = 2$ refers to its counterpart.

The mesh sizes considered for this case are laid out in Table 1. In addition to the regular discretization method, we also consider a mesh

Table 1
Mesh sizes considered for the convergence study.

Name	FE mesh			BE mesh
	Size (m)	Formulation	Type	Size (m)
A	0.50	Reduced	Regular	0.50
B	0.50	Linear	Regular	0.50
C	0.50	Quadratic	Regular	0.50
D	0.50	Quadratic	Regular	0.40
E	0.35	Linear	WL86	0.40
F	0.40	Quadratic	WL86	0.40
G	0.35	Quadratic	WL86	0.40

bias following the work by Wong and Luco [12] (marked as WL86 in the table). Such a discretization method is important to capture the stress concentration around the soil–foundation interfaces' edges that arise due to the foundations' sharp corners. Following and modifying the concept by Wong and Luco, the foundations and the soil underneath are discretized horizontally into 16×16 grid. The sizes of the elements, starting from an edge to a mid-line of a foundation, are defined as

$$\Delta_j = b\frac{\alpha^{(j-1)}}{\sum_{j=1}^{8}\alpha^{(j-1)}}, \text{for } j = 1, 2, \ldots, 8. \tag{12}$$

The constant α controls the contrast between the elements' sizes, and we chose $\alpha = 1.5$. Sizes 0.5, 0.4, and 0.35 in Table 1 correspond to Δ_8, and they are 1/3.1, 1/3.9, and 1/4.5 of the shortest wavelength at a frequency of 0.64 Hz, respectively. Note that this frequency results in $a_0 \approx 4$ for the aforementioned material properties and $b = 1$ m. The bias is also used to discretize the soil region surrounding the foundations. These sizes in Table 1 are also used to mesh in the vertical direction without bias. In the regular FE mesh type, the element sizes shown in the table are applied to all finite elements without bias.

The finite region is meshed using hexahedral elements with either linear (C3D8), quadratic (C3D20), or "reduced" (C3D8R) formulation. The latter refers to an element type with one integration point, i.e., a constant element. The BE model is meshed using linear quadrilateral shell elements (S4).

A comparison of compliance functions between our numerical results with the ones by Karabalis and Mohammadi [17] is shown in Fig. 5(a). Note that the latter was obtained using constant boundary elements, a regular discretization technique, and relaxed boundary conditions on the soil–foundation contact. The contact definition is adapted to our numerical model for this particular part of the study. The results are for a distance-to-half-width ratio, d/b, of 2 and β of 5%. The hybrid BEM-FEM model results in a similar trend but lower compliances (or higher impedances) compared to the existing solution, even when using constant elements and a regular discretization technique (Mesh A). Reducing the element size and increasing the number of integration points lead to an oscillation of the results towards convergence (Fig. 5(b)), which is contrary to expectation. However, even though the compliances obtained from Mesh A and Mesh G seem to be similar, they differ significantly in terms of wave dispersion, as can be seen in the results visualizations in Fig. 6. The wave field result obtained from Mesh A shows a reasonable waveform but lacks the deformation details. The loaded foundation's displacement response to a unit harmonic load from Mesh A and Mesh G are (0.44+i6.21)E-2 m and (−1.43+i5.73)E-2 m, respectively. Thus, it can be examined that Mesh A results in a shifted response relative to the results from Mesh G. Hence, the similarities and oscillation found in Fig. 5 can be explained by the fact that the compliance functions merge the real and imaginary parts and may give an incomplete picture. The influence of the discretization technique on the simulation result can be seen by comparing the results from Mesh D with the ones from Mesh E or Mesh F (Fig. 5(b)). The results from Mesh F and Mesh G show that convergence is likely achieved. Based on these results, Mesh G is used as the main setup for the parametric study.

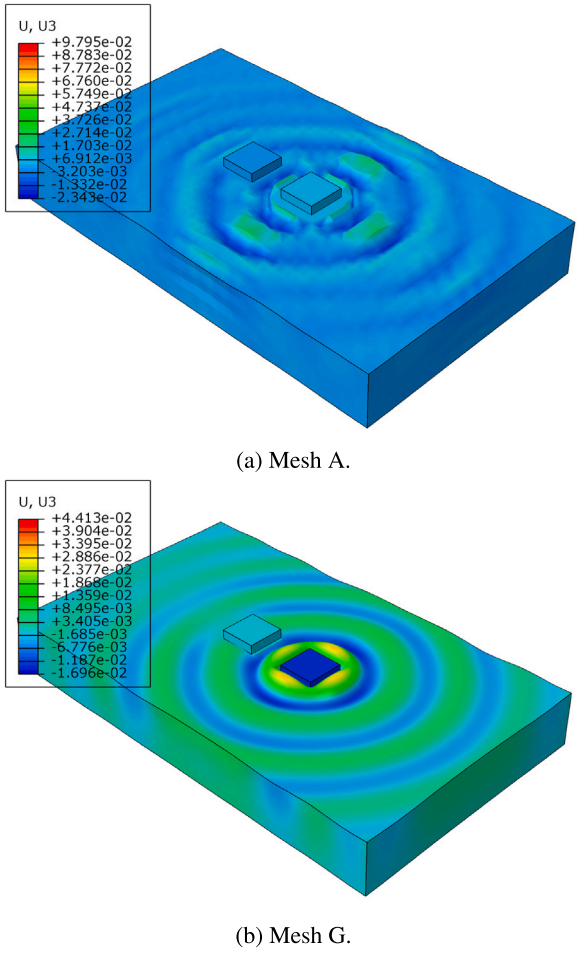

(a) Mesh A.

(b) Mesh G.

Fig. 6. Visualized wave fields (real part) for Mesh A and Mesh G at a $a_0 = 2.0$. Units in meter.

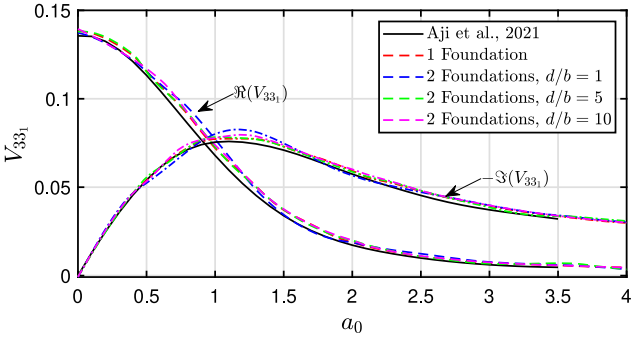

Fig. 7. Comparison of vertical compliance functions obtained from models with one load-sustaining foundation for varying distance between foundations.

The results in Figs. 5 and 6 show the importance of the discretization technique, mesh sizes, and mesh formulation to the solution's accuracy. By gradually decreasing the mesh sizes, applying a mesh bias to obtain a finer mesh near the foundations' edges, and using higher-order interpolation functions, it can be seen that the results are improved towards convergence. Examination of the displacement fields surrounding the foundation also reveals the presence of shorter wavelengths, which means that the finer mesh and higher order interpolation surrounding the foundations' edges serve not only to approximate the stress concentration but also to capture the shorter waveforms.

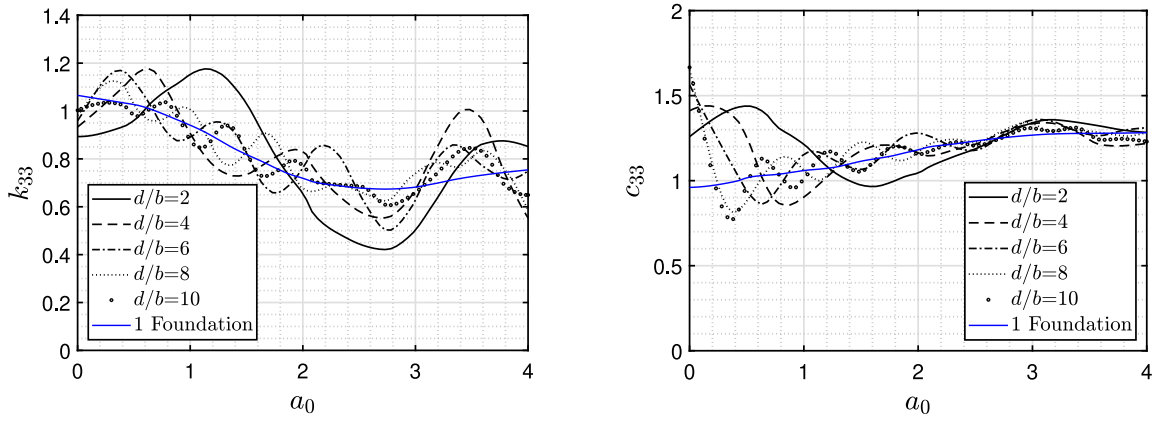

(a) k_{33} vs. a_0. (b) c_{33} vs. a_0.

Fig. 8. Influence of d/b on impedance coefficients ($\nu = 1/3$, $l/b = 1$, $\beta = 0\%$, $\phi = 0°$).

Both points, otherwise, cannot be achieved using a regular meshing technique and constant elements.

The discretized surface's width in the BE model is chosen to be two meters (Fig. 2(b)). A previous numerical experiment on this method in [39] showed that a good accuracy can be obtained by keeping the ratio between the longest shear wavelength, λ_S, and the discretized surface of the half-space, l_{Γ_B}, below 500, i.e., $\lambda_S/l_{\Gamma_B} \leq 500$. For the lowest considered frequency of 5E-3 Hz, the width leads to a ratio of 100.

The convergence study is extended for models with varying distances between foundations, d, and the results are compared with the ones obtained from a model with a single foundation using mesh setup Mesh G. In addition, the results are compared with the ones presented in [21]. Compared to the results in [21], the simulations performed in this study for a single foundation using Mesh G results in slightly higher compliances, as shown in Fig. 7. This is because the results in [21] were obtained using a regular meshing technique. By increasing d/b, the results obtained from models with two foundations, in which only one of them is subjected to a harmonic load, are converging towards the results obtained from a single-foundation model, which is as expected. The mean absolute differences between the compliances' real part from $d/b = 1$, 5, and 10 relative to the one from the single-foundation model are 6.32%, 4.77%, and 2.05%, respectively. The corresponding values for the imaginary part are 2.63%, 1.74%, and 1.17%, respectively. It can be also concluded that the influence of a second foundation in this case is rather minimal beyond a d/b ratio of 5.

4. Numerical study results and discussions

The parametric study is focused on understanding the response of adjacent rectangular foundations when both are experiencing dynamic loads concurrently. The typical model geometry used for the parametric study is as shown in Fig. 2. The parameters considered are as follows: the clear distance between foundations, normalized to the foundations' half-width, d/b; material damping, β; Poisson's ratio, ν; the shape ratio of the rectangular foundations, presented as l/b; and the phase angle between the harmonic loads acting on the foundations, ϕ. The illustration of the dimensions b, d, and l can be found in Fig. 1. The range of these parameters is chosen to represent mainly structures with closely spaced foundations or short-to-medium span frame bridges and is given in Table 2. The parametric study is performed by maintaining the material properties as before ($C_S = 1$ m s^{-1}, $\rho = 1$ kg m^{-3}, $\mu = 1$ Pa) and a foundation half-width, b, of 1 m. The magnitude of the vertical harmonic loads, $|P_3|$, is 1 N. For each soil–foundations setup, simulations are performed for a frequency range of [0.005, 0.64] Hz.

The results of the parametric study are presented in the form of impedance and compliance values shown in classical 2D plots and 3D surfaces. The latter provides completeness, and these two combined perspectives facilitate a better understanding of the system's response. The 3D surfaces are also preferable for practical engineering purposes due to the complexity of the system's response, and they are available online at https://doi.org/10.57892/100-50. A calculation example is given in Appendix.

Table 2
Range of parameters considered for the parametric study. The illustration of d, b, and l is given in Fig. 1.

Parameter	Range or values
d/b	0.1–10
β	0%, 5%, 10%
ν	1/3, 0.40, 0.49
l/b	1–4
ϕ	(−180°)–180°

4.1. Influence of the distance between foundations

The impedance coefficients, k_{33} and c_{33}, for varying foundations' distance ratio, d/b, values and $\nu = 1/3$, $l/b = 1$, and $\phi = 0°$ are presented in Figs. 8(a) and 8(b). The simulations are performed for a variety of d/b values in a grid of 0.5, and the results are then organized into impedance coefficients surfaces and a compliance surface as shown in Figs. 9(a)–9(c).

Figs. 8 and 9 show that an increase in the distance between foundations leads to an additional number of peaks in the foundation's response, which is dissimilar to the case of two adjacent foundations when only one of them is receiving a harmonic load, see [18]. Figs. 9(a) and 9(b) illustrate the influence of d/b on the real and imaginary parts coefficients of the impedance, while Fig. 9(c) shows the resonance patterns in the compliance surface. The trend of decreasing resonance frequency as d/b increases can be observed here. It can also be observed in Fig. 9 that these patterns of resonance occur as a result of the interaction between the foundation arrangement, excitation frequency, and soil properties. These patterns can be related to the shear or Rayleigh wavelength as is done in Wolf [43], who describes the FSFI of pile foundations ($\varnothing = 2r_0$) in terms of the ratio of the shear wavelength, λ_S, to the pile spacing, d_p. In this context, it was observed that the resonant inertia (mass) results in a reduction of the real part of the impedance function as the frequency increases. However, in the case of group foundations, this reduction is interrupted by the progressive predominance of the shear wave ($\lambda_S \rightarrow d_p$) between the piles. Once the threshold is reached, the soil experiences an increasingly pronounced antiphase oscillation, resulting in a significant decrease in stiffness. The

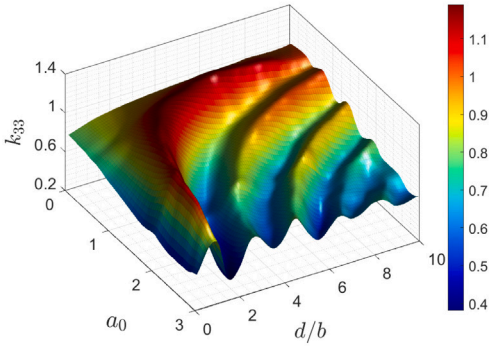

(a) k_{33} vs. a_0 vs. d/b.

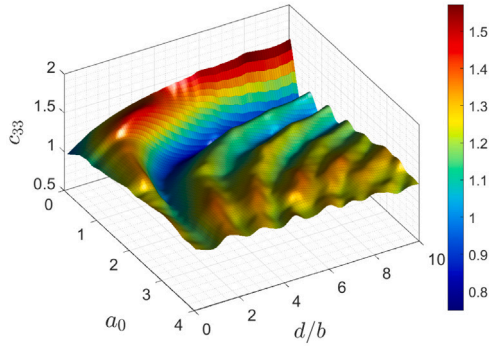

(b) c_{33} vs. a_0 vs. d/b.

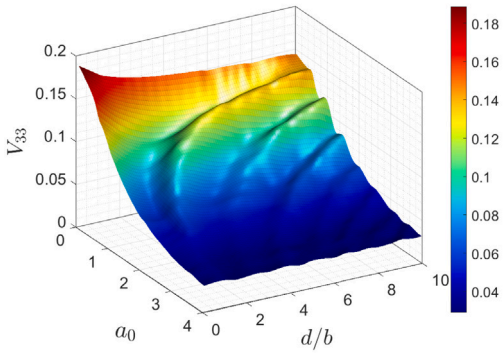

(c) V_{33} vs. a_0 vs. d/b.

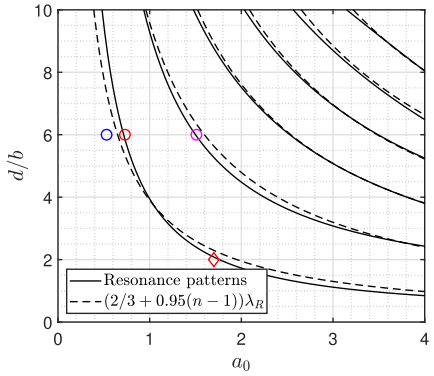

(d) Curves fitted to the resonance patterns in Fig. 9c.

Fig. 9. Influence of d/b on impedance and compliance surfaces ($\nu = 1/3$, $l/b = 1$, $\beta = 0\%$, $\phi = 0°$).

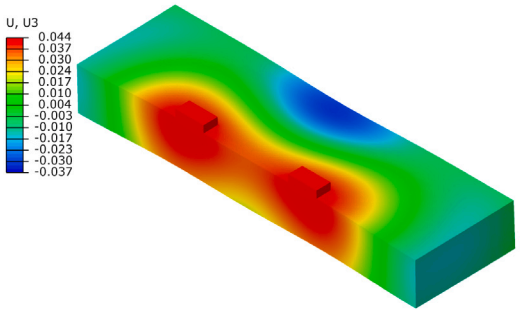

(a) $\Im(u_3)$ at $a_0 = 0.53$.

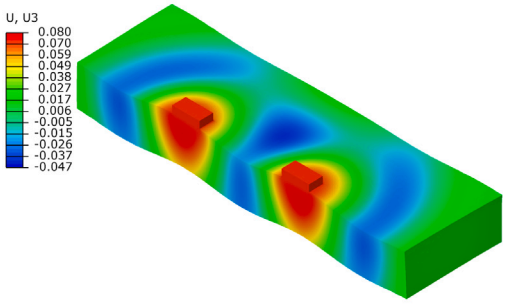

(b) $\Im(u_3)$ at $a_0 = 0.73$.

Fig. 10. Vertical displacement fields (imaginary part) obtained from models with $d/b = 6$, illustrating wave patterns at a_0 (a) lower than and (b) within the first resonance frequency. Other parameters are $l/b = 1, \nu = 1/3, \beta = 0\%$, and $\phi = 0°$. Units in meter.

nth nadir of the real part of the impedance at $a_{0(n),r}$ is reached when both piles oscillate out of phase.

$$a_{0(n),r} = \frac{2\pi r_0}{d_p}(1 + 0.5n) \text{ with } n \in \mathbb{Z}^+. \tag{13}$$

A similar form to Eq. ((13)) can be obtained for the displacement or compliance peaks in the context of rectangular foundations ($r_0 \to b$ and $d_p \to d$). Fig. 9(d) shows that the resonance patterns can be approximated using the relation

$$\frac{d}{b} = \left(\frac{2}{3} + 0.95(n-1)\right)\lambda_R \text{ with } n \in \mathbb{Z}^+. \tag{14}$$

Here, λ_R is the Rayleigh wavelength. Writing for a_0, the following approximation for the nth resonance line is obtained:

$$a_{0(n)} = \frac{\pi b}{d}\frac{C_R}{C_S}\left(\frac{4}{3} + 1.9(n-1)\right) \text{ with } n \in \mathbb{Z}^+. \tag{15}$$

Alternatively, one can reach a similar approximation accuracy without using the Rayleigh wave velocity, C_R, by using

$$a_{0(n)} = \frac{\pi b}{d}\left(\frac{5}{4} + 1.8(n-1)\right) \text{ with } n \in \mathbb{Z}^+. \tag{16}$$

Note that in the formulae above, the influence of soil properties on the resonance frequency is included in the term a_0.

By examining the displacement fields, the relation between the resonance patterns and the phase difference between the foundations' response and that of a partitioned soil volume between foundations can be observed. This argument is illustrated in Fig. 10, which shows the imaginary vertical displacement fields for models with $d/b = 6$. Fig. 10(a) shows the displacement fields at a_0 lower than the first resonance frequency, while Fig. 10(b) shows those within it. The positions of these values are shown by blue and red circles, respectively, in Fig. 9(d). These figures illustrate that the system starts to enter

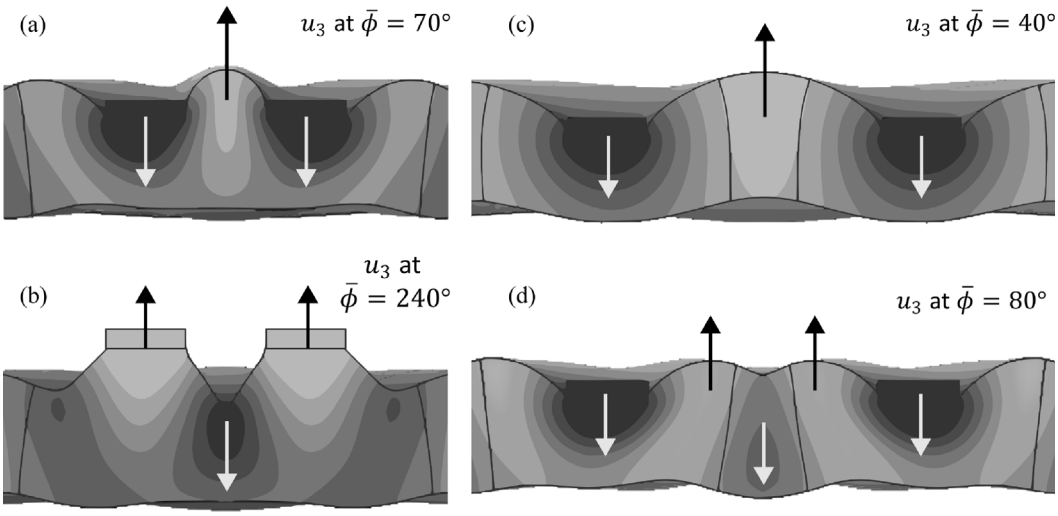

Fig. 11. Displacement pattern of twin surface foundations under synchronous harmonic loads during resonance states: Results from model with $d/b = 2$ at $a_0 = 1.7$ showing u_3 at output phases corresponding to (a) the foundations' minimum vertical displacement ($\bar{\phi} = 70°$) and (b) the foundations' maximum vertical displacement ($\bar{\phi} = 240°$); results from model with $d/b = 6$ at (c) the first resonance frequency ($a_0 = 0.73$) and (d) the second resonance frequency ($a_0 = 1.51$) showing u_3 at output phases corresponding to foundations' minimum vertical displacements. Other parameters are $l/b = 1$, $\nu = 1/3$, $\beta = 0\%$, and $\phi = 0°$.

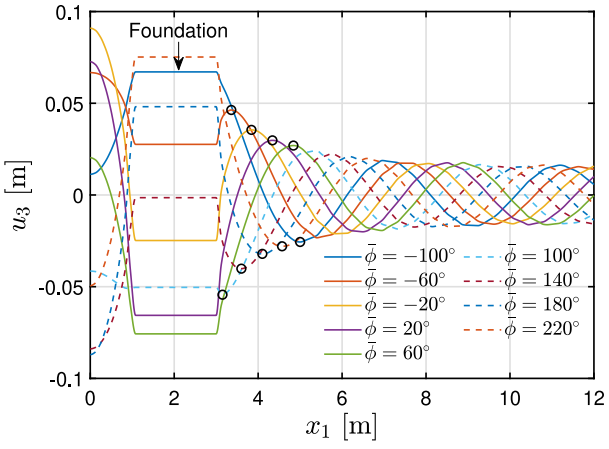

Fig. 12. Vertical displacements for varying output phases, $\bar{\phi}$, along the line $x_2 = x_3 = 0$ obtained from a model with $d/b = 2$, $l/b = 1$, $\nu = 1/3$, $\beta = 0\%$, and $\phi = 0°$ at $a_0 = 1.39$. Black circles mark the start of the Rayleigh waves.

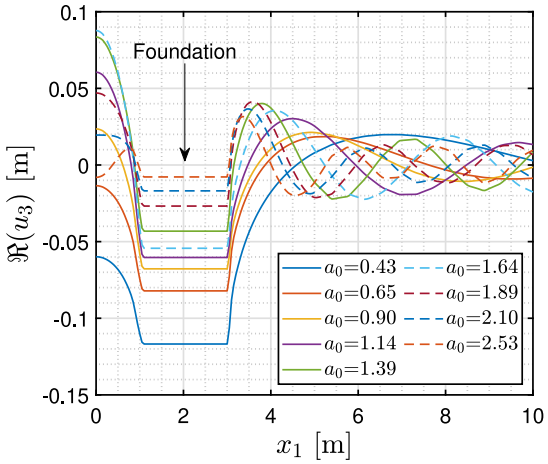

Fig. 13. Vertical displacements (real part) along the line $x_2 = x_3 = 0$ at varying a_0 obtained from models with $d/b = 2$, $l/b = 1$, $\nu = 1/3$, $\beta = 0\%$, and $\phi = 0°$.

the first resonance pattern when the partitioned soil volume between foundations starts to move out of phase relative to the foundations' response, similar to an MDOF system. The peak resonance then occurs when the phase difference between the response of the soil wedge and the foundations is 180°. The phase differences in these 2 figures are 121° and 181°, respectively, and these values are measured at the foundations and the center of soil wedge between foundations shown in Fig. 10(b). Although certain soil regions surrounding both foundations move in phase with the soil wedge between foundations (Fig. 10(b), blue areas outside both foundations), results obtained from the simulation of a single foundation show that their movement does not lead to resonance.

The kinematics of the system is further detailed in Fig. 11. The displacement fields from a model with $d/b = 2$ at output phases corresponding to foundations' minimum and maximum vertical displacements are shown in the left figures. It can be observed that the soil wedge between foundations experiences a shape transition during the oscillation. The wave fields from models with $d/b = 6$ at different resonance frequencies are plotted on the right figures. They show that the resonance at a higher frequency occurs when the soil volume between foundations is partitioned further into smaller parts that move at a phase of 180° to each other. For $d/b = 6$, the first resonance frequency occurs at $(d/b)/\lambda_S \approx 0.70$ and the second one occurs at $(d/b)/\lambda_S \approx 1.44$ (see Fig. 9(c), magenta circle).

The form-finding of the partitioned soil wedge between foundations is influenced by the distortion zone around the foundations, which is the result of the kinematic and inertial interactions between the rigid foundation and the soil. Fig. 12 shows the vertical displacement fields obtained from a model with $l/b = 1$, $\nu = 1/3$, and $\beta = 0\%$ at excitation frequency $a_0 = 1.39$. The displacements are plotted for varying output phases relative to their real value, $\bar{\phi}$. The figure illustrates the surface wavelengths on the far-field direction ($x_1 > 3$) and on the region facing the other foundation ($0 \leq x_1 < 1$). The distortion zone lies between the foundation's edge and the starting point of the Rayleigh wave. In the figure, the starting point of each output phase's Rayleigh wave is marked with a black circle. It can be observed that the distortion zone for a certain frequency or wavelength depends on the foundation's position during its harmonic motion and that the distortion zone extends from the edge of a foundation to approximately a half of the Rayleigh wavelength, λ_R, which in this case is 4.20 m. The figure also shows the shorter wavelength appearing within the distortion zone. This supports the result of the mesh convergence study that a finer mesh is required

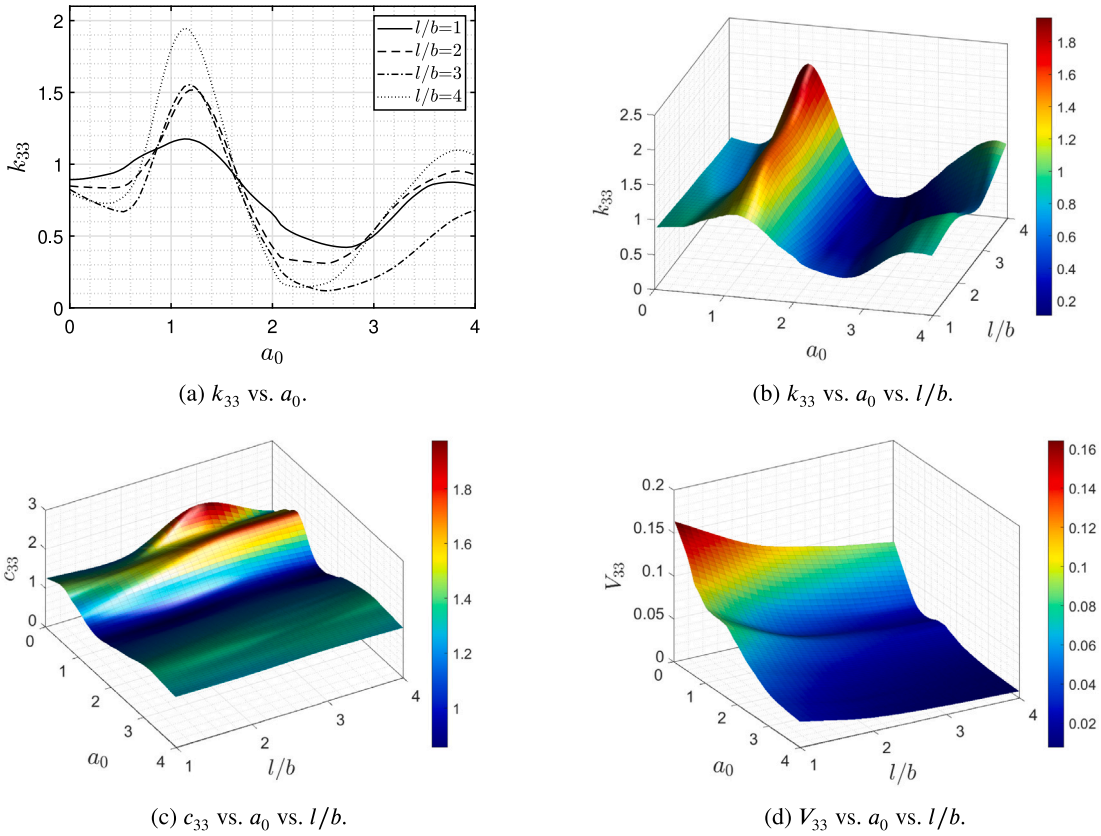

(a) k_{33} vs. a_0.

(b) k_{33} vs. a_0 vs. l/b.

(c) c_{33} vs. a_0 vs. l/b.

(d) V_{33} vs. a_0 vs. l/b.

Fig. 14. Influence of l/b on impedance and compliance function and surfaces ($d/b = 2$, $\nu = 1/3$, $\beta = 0\%$, $\phi = 0°$).

in the vicinity of the foundation, which would ensure that the shorter wavelengths can be sufficiently approximated.

Fig. 13 presents the real part of vertical displacements along the line $x_2 = x_3 = 0$ from models of two foundations with $d/b = 2$ at varying a_0. It can be observed that the interaction between two foundations results in a consistent wave pattern in the zone between foundations for a wide range of excitation frequency, i.e., $0 < a_0 \leq 1.64$. The wave pattern is modified when the system enters and subsequently leaves its resonance state ($a_{0(1)} = 1.7$, see Fig. 9(d), red diamond marker). Upon examination of the results for varying output phases at $a_0 = 1.39$, shown in Fig. 12, it can be observed that this wave pattern between foundations remains consistent regardless of the output phases, unlike the wave pattern in the far-field direction. Thus, Figs. 12 and 13 show that the behavior of the partitioned soil wedge between foundations is related to the resonance patterns. In the practical field, this implies that the material properties of the region between the foundations play a significant role in the foundations' behavior.

4.2. Influence of the foundation's shape ratio

The foundation's geometry is represented here as a ratio between its half-length and half-width, l/b. The length l is measured perpendicular to the distance between the foundations d, see Fig. 1. The impedance and compliance surfaces from models with $l/b = [1, 4]$ and $\nu = 1/3$, $\beta = 0\%$, $\phi = 0°$ are presented in Fig. 14. Fig. 14(a) shows that dissimilar to the case of a single foundation, the ratio l/b tends to have an amplifying influence on the impedances' real coefficients with local minima found along $a_0 = [0.30, 0.58]$ and $a_0 = [2.08, 2.58]$. On the other hand, Fig. 14(c) depicts that the ratio has a complex influence on the imaginary parts of the impedances in the low-frequency regime with a higher value found in the vicinity of $l/b \approx 3$. Fig. 14(d), however, shows that there is hardly any change in the resonance frequency. This result is consistent with the results obtained from models with only one load-sustaining foundation, see [18]. This suggests that the changes in the impedance coefficients due to the change of l/b do not alter the kinematics of the system and the increase in the participating soil mass is proportional to the increase in the dynamic stiffness. The figure also shows that compliance tends to exponentially decrease as l/b value increases. Considering that the half-length of the foundation, l, is not taken into account in the derivation of V_{33} (see Eq. (2)), this effect can be understood simply as the result of a larger spread of the energy.

The impedance surfaces obtained from models with $d/b = 4$ and 6 are presented in Fig. 15. The figure shows that a similar amplification effect is present in the impedances' real coefficient surfaces, albeit with a different magnitude (see the highest values shown in the scale bar in Figs. 14(b), 15(a), and 15(c)). Figs. 14 and 15 also show that foundations with l/b ratio of around 3 consistently result in lower in-phase coefficients (real part of the impedances) at a high-frequency range and higher imaginary coefficients at a lower frequency range.

Further examination of the displacement fields reveals that increasing l/b induces an inconsistent shape transition of the soil volume between foundations, which is crucial in the system's resonance. This is rather intriguing since the inconsistent shape transition does not influence the resonance frequency, as shown in Fig. 14(d). Fig. 16 presents the real part of vertical displacement fields for varying l/b values at a resonance frequency. It can be observed by comparing Figs. 16(a) and 16(b) that increasing the shape ratio from $l/b = 1$ to $l/b = 2$ elongates the soil wedge between foundations. However, models with $l/b = 3$ and 4 result in partitioned soil regions with two smaller ellipsoids rather than an elongated one, which suggests the predominance of the shear or surface wavelength on the region between foundations. This inconsistency may relate to the shift in the local minima found in Fig. 14(a). This fact also suggests that a plane strain approach for long rectangular foundations has to be taken carefully when the wave dispersion is of interest. However, the compliance function results in

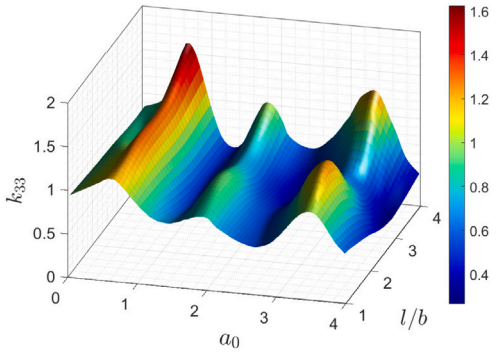

(a) k_{33} vs. a_0 vs. l/b for $d/b = 4$.

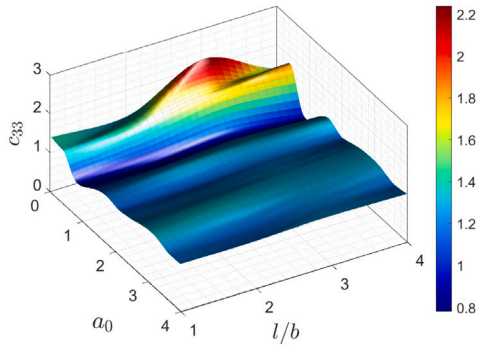

(b) c_{33} vs. a_0 vs. l/b for $d/b = 4$.

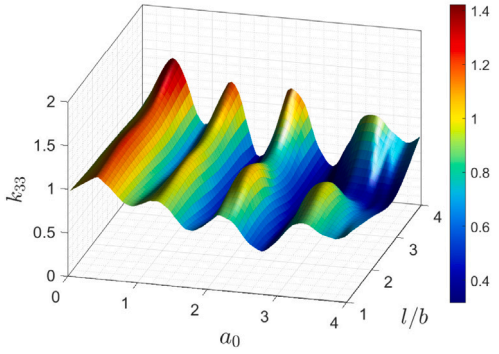

(c) k_{33} vs. a_0 vs. l/b for $d/b = 6$.

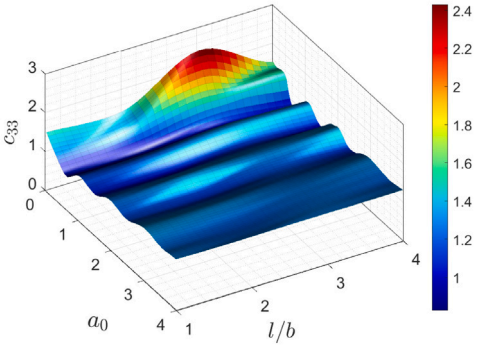

(d) c_{33} vs. a_0 vs. l/b for $d/b = 6$.

Fig. 15. Influence of l/b on impedance surfaces for $d/b = 4$ and 6 ($\nu = 1/3$, $\beta = 0\%$, $\phi = 0°$).

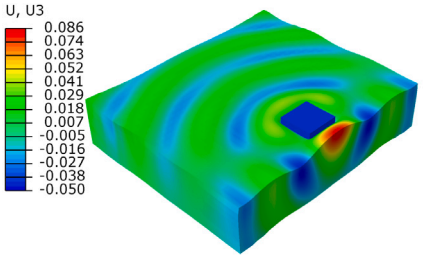

(a) $\Re(u_3)$ obtained from model with $l/b = 1$.

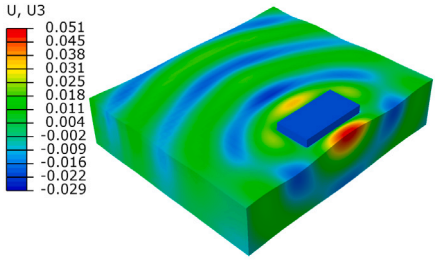

(b) $\Re(u_3)$ obtained from model with $l/b = 2$.

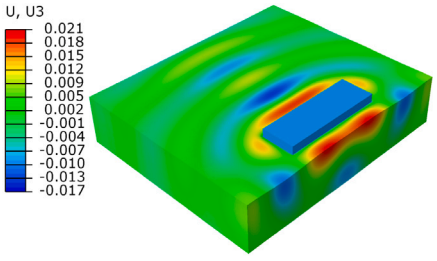

(c) $\Re(u_3)$ obtained from model with $l/b = 3$.

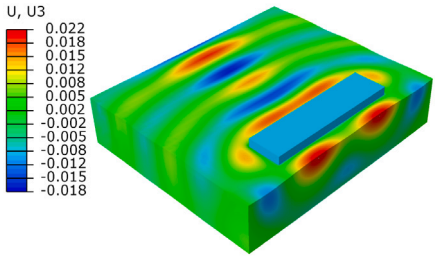

(d) $\Re(u_3)$ obtained from model with $l/b = 4$.

Fig. 16. Vertical displacement fields (real part) obtained from models with varying l/b values at $a_0 = 1.64$ and with $d/b = 2$, $\nu = 1/3$, $\beta = 0\%$, and $\phi = 0°$. Units in meter.

Fig. 14(d) suggest that the foundation's response produced by such an approach may still be accurate. Further comparative study on this point is suggested to form a more reliable conclusion. Note that when approaching dynamic problems from a 2D perspective, one still has to account for the damping paradox as discussed in [23].

4.3. Influence of Poisson's ratio

The impedance and compliance functions and surfaces for higher Poisson's ratios $\nu = 0.40$ and $\nu = 0.49$ and for varying d/b are presented in Fig. 17. Other material properties, i.e., C_S, ρ, and μ, are kept the

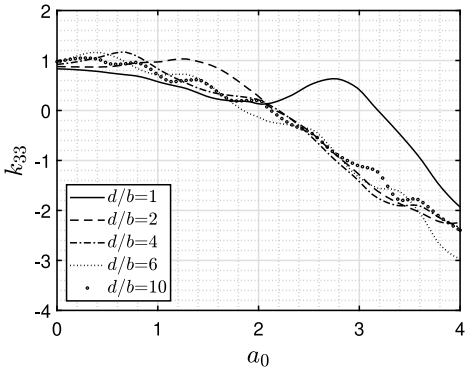

(a) k_{33} vs. a_0 for $\nu = 0.49$.

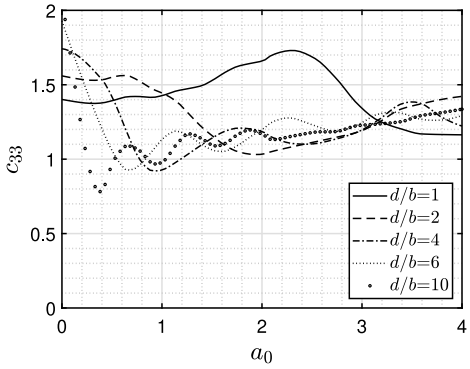

(b) c_{33} vs. a_0 for $\nu = 0.49$.

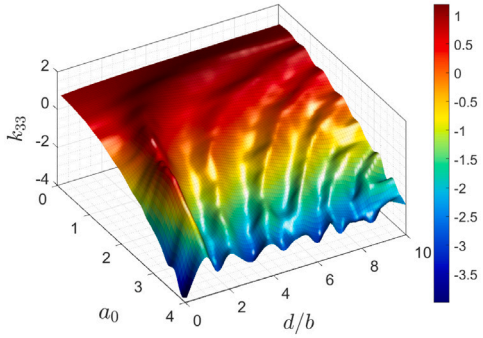

(c) k_{33} vs. a_0 vs. d/b for $\nu = 0.49$.

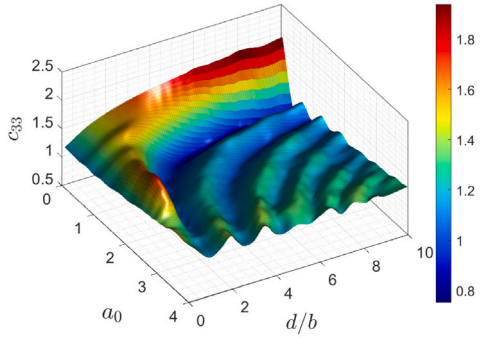

(d) c_{33} vs. a_0 vs. d/b for $\nu = 0.49$.

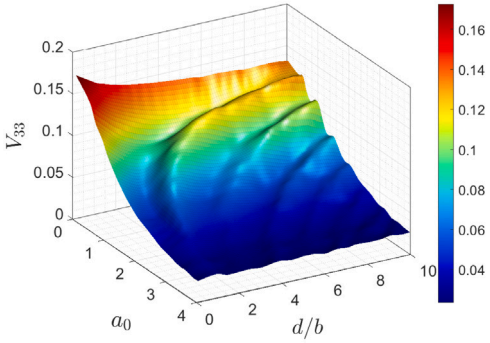

(e) V_{33} vs. a_0 vs. d/b for $\nu = 0.40$.

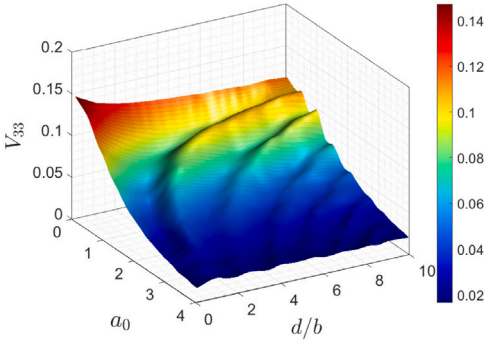

(f) V_{33} vs. a_0 vs. d/b for $\nu = 0.49$.

Fig. 17. Influence of d/b on impedance and compliance functions and surfaces for $\nu = 0.40$ and $\nu = 0.49$ ($l/b = 1$, $\beta = 0\%$, $\phi = 0°$).

same as before. Further examination shows that the resonance lines in Fig. 17(e) are the same as those appearing in Fig. 9(c), while the resonances in Fig. 17(f) are shifted in the $+a_0$-direction by approximately 0.05 relative to those in Fig. 9(c). This suggests the minor influence of the Poisson's ratio and that Eq. (15) would be more suitable for a higher Poisson's ratio.

The impedance coefficients obtained from the models with $d/b = 2$, $l/b = 1$, $\phi = 0°$, $\beta = 0\%$, and with $\nu = 1/3$, 0.40, and 0.49 are compared in Figs. 18(a) and 18(b); they are interpolated into impedance and compliance surfaces in Figs. 18(c) and 18(d). It can be observed that the influence of Poisson's ratio on the real and imaginary parts is as expected and similar to the one for the case of a single foundation, e.g., in [37]. Although the influence of Poisson's ratio on the impedance's real part surface varies for different frequency ranges (Fig. 18(c)), higher Poisson's ratio tends to result in a consistent decrease in the foundation's response for all frequency range as shown in Fig. 18(d). The figure also shows that the resonance frequency remains the same as ν increases. The influence of larger Poisson's ratio is already known and well described for single foundations. Wolf [43] describes this effect in terms of a trapped mass, which leads to a continuous decrease in the real component of the impedance function with increasing frequencies, as the inertia counteracts the stiffness. Very similar correlations can be observed in Fig. 18(a). Conversely, the higher incompressibility of a media with a high Poisson's ratio increases the static stiffness (see Eq. (9)), which overcompensates the decrease in the in-phase impedance coefficients and, thus, reduces the displacement responses.

Fig. 19 shows the effect of increasing Poisson's ratios on the Rayleigh wavelengths and on the foundations' stiffness, as a result of the increase in incompressibility.

4.4. Influence of material damping

In the case that a non-zero material damping is included in the system, Eq. (4) is written as [36]

$$S_{jk}(\omega) = K_{jk}k_{jk}(\omega) - \omega\beta C_{jk}c_{jk}(\omega) + i\left(\omega C_{jk}c_{jk}(\omega) + 2\beta K_{jk}k_{jk}(\omega)\right). \quad (17)$$

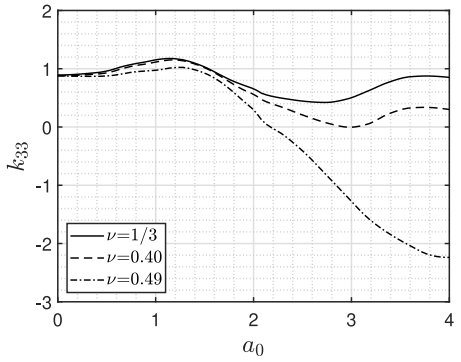

(a) k_{33} vs. a_0.

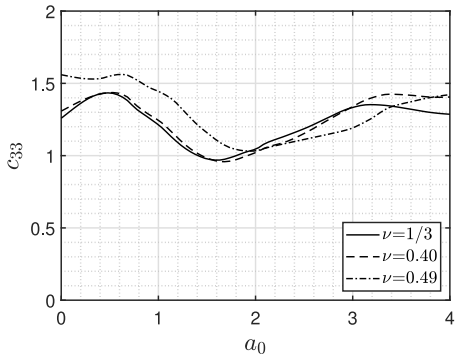

(b) c_{33} vs. a_0.

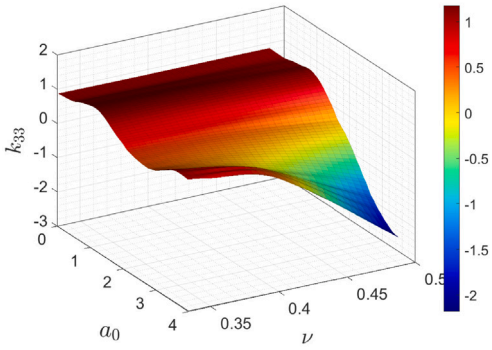

(c) k_{33} vs. a_0 vs. ν.

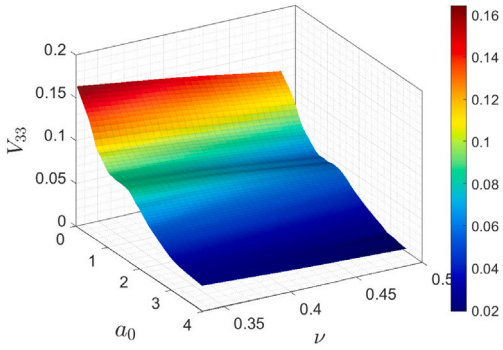

(d) V_{33} vs. a_0 vs. ν.

Fig. 18. Influence of Poisson's ratio ν on impedance and compliance functions and surfaces ($d/b = 2$, $l/b = 1$, $\beta = 0\%$, $\phi = 0°$).

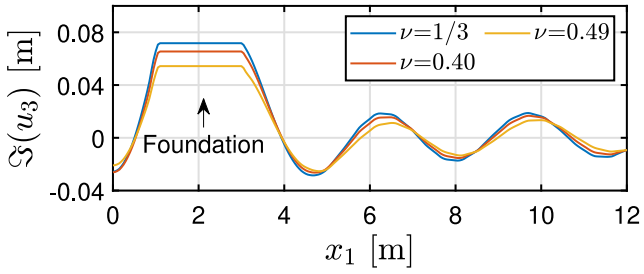

Fig. 19. Vertical displacements (imaginary part) along the line $x_2 = x_3 = 0$ obtained from models with varying ν and with $d/b = 2$, $l/b = 1$, $\beta = 0\%$, and $\phi = 0°$.

To investigate the effect of material damping on the impedances, the dynamic coefficients obtained from undamped cases are modified to the damped ones, $k_{jk}(\omega, \beta^*), c_{jk}(\omega, \beta^*)$, by the following relations:

$$k_{jk}(\omega, \beta^*) = \frac{\Re\left(S_{jk}(\omega)\right) - \omega\beta\Im\left(S_{jk}(\omega)\right)}{K_{jk}} \quad \text{and} \tag{18}$$

$$c_{jk}(\omega, \beta^*) = \frac{\Im\left(S_{jk}(\omega)\right) + 2\beta\Re\left(S_{jk}(\omega)\right)}{\omega C_{jk}}. \tag{19}$$

The damping-modified impedance functions for varying d/b values, computed from undamped coefficients using the above relations, are compared with those obtained from models with material damping values, β, of 5% and 10% in Fig. 20. The modified and damped in-phase coefficients fit quite well to each other for cases with $d/b = 2$ and $\beta = 5\%$ but the coefficients obtained from other cases show a good agreement only in the low-frequency regime (Fig. 20(a)). On the other hand, Fig. 20(b) shows very good agreements between the imaginary coefficients for all cases. The relative differences between the in-phase coefficients are quantified in Fig. 20(c). Taking into account the results in Sections 4.1 and 4.2, the contrast in the approximation accuracies between the real and the imaginary parts can be understood as the complex influence of the mass of the partitioned soil volume between the foundations. This can be illustrated by an examination of Eq. (17). When mass, m, is included there, the real part of the impedance is modified by the term $-\omega^2 m$, while the imaginary one is unchanged. However, we find that a consistent pattern cannot be obtained by taking the differences between the damping-modified impedances and damped ones. As an alternative, the real part of undamped impedances can be fitted to the damped impedances better in the higher frequency regime when the coefficients of the former are modified using the following relation:

$$k_{jk}(\omega, \beta^*) = \frac{\Re\left(S_{jk}(\omega)\right)}{K_{jk}\left(1 + 2\beta a_0\right)}. \tag{20}$$

Fig. 21 shows that the modified in-phase impedance coefficients, obtained using the above relation, fit quite well with the ones for damped cases up to $a_0 = 2.8$. The maximum relative differences are shown to be decreased to below 20%. Thus, Eq. (17) is modified for cases involving non-zero material damping into

$$S_{jk}(\omega) = \frac{K_{jk}k_{jk}(\omega)}{\left(1 + 2\beta a_0\right)} + i\left(\omega C_{jk}c_{jk}(\omega) + 2\beta K_{jk}k_{jk}(\omega)\right). \tag{21}$$

This illustrates the complex influence of the inclusion of material damping on the impedance coefficients.

4.5. Influence of the phase shift between harmonic loads

In adjacent foundations of structures such as bridges or machinery, asynchronous harmonic loads may occur due to the nature of the passing vehicle or the operation sequence. A positive phase on a foundation here can be understood as the foundation sustaining a slightly delayed harmonic loading, relative to a reference foundation, while a negative

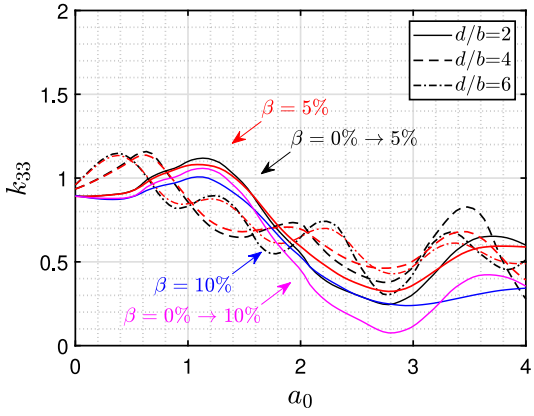

(a) k_{33} vs. a_0.

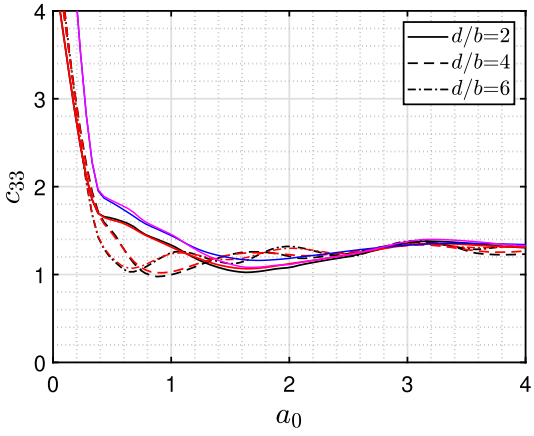

(b) c_{33} vs. a_0.

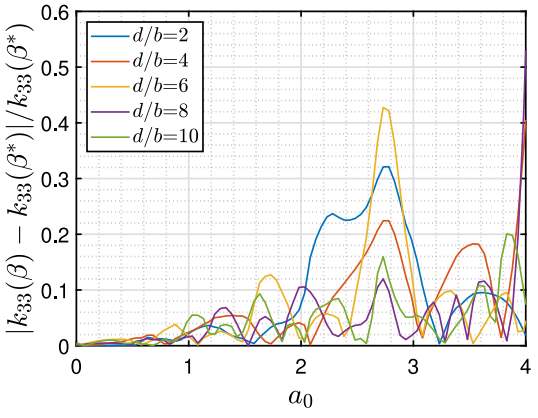

(c) $|k_{33}(\beta) - k_{33}(\beta^*)|/k_{33}(\beta^*)$ for $\beta = 5\%$.

Fig. 20. Comparison between impedances modified from models with zero material damping and those obtained from models with non-zero material damping ($\nu = 1/3$, $l/b = 1$, $\phi = 0°$).

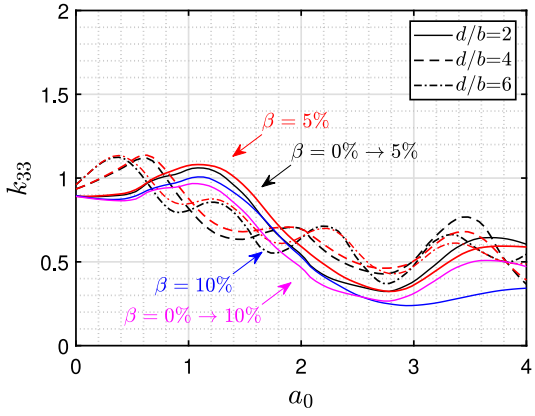

(a) k_{33} vs. a_0.

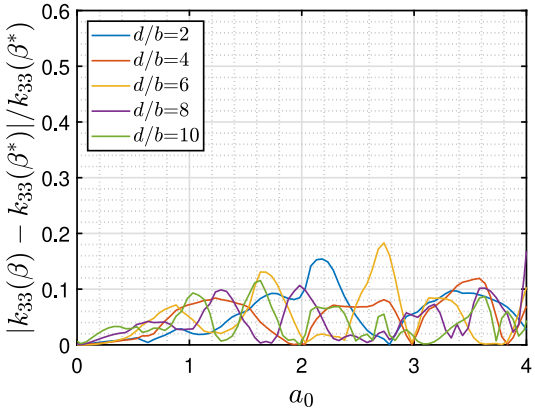

(b) $|k_{33}(\beta) - k_{33}(\beta^*)|/k_{33}(\beta^*)$ for $\beta = 5\%$.

Fig. 21. Improved in-phase coefficients, k_{33}, modified from the results of models with zero material damping using Eq. (18) ($\nu = 1/3$, $l/b = 1$, and $\phi = 0°$).

phase refers to the opposite experience of the reference foundation (see Fig. 3). Thus, the result of a simulation with a phase ϕ between the harmonic loads can be plotted from the perspective of either the reference or the second foundation.

Fig. 22 presents the impedance (real part) and compliance surfaces for varying d/b cases where a shift in the harmonic load is applied on one foundation. The impedances and compliances shown in the figure are measured on the reference foundation which sustains no shift in its load. Thus, the results can be read as the response of a foundation under a harmonic load when a nearby foundation is receiving a load with a phase shift but with the same magnitude and frequency. Data points for $d/b = 5$ are shown in Figs. 22(a) and 22(b), which show that the real coefficient peaks are shifted accordingly. The a_0 value related to $d/b = 5$ is shifted from 0.53 in Fig. 9(a) to 0.68 and 0.98 for cases with $\phi = -90°$ and $-180°$, respectively. Note that these points are related to the valleys in the corresponding compliance plots in Figs. 22(c) and 22(d). These last two figures also show new discontinuous resonance patterns forming along the low frequency regime at $a_0 \approx 0.4$–0.6 (see Fig. 22(d), yellow dashed line).

The impedance and compliance function and surfaces from the simulations with $d/b = 2$, $\nu = 1/3$, $l/b = 1$, $\beta = 0\%$, and $\phi = [-180, 180]$ are examined in Fig. 23. The surfaces can be read as the response of a foundation under a vertical harmonic load when a nearby adjacent foundation sustains a similar load with either a positive or a negative phase shift. It is shown in Figs. 23(b)–23(d) that a positive phase applied on the second foundation's load tends to shift the response pattern of the reference foundation towards a lower frequency, and a negative phase tends to have the opposite effect. The rates of change $\Delta a_0/\Delta\phi$ along the resonance frequencies in the positive and negative phase directions are found to be approximately -1/450. However, the influence of the phase shift on the compliance surface tends to be damped at a higher frequency range (Fig. 23(d)). The decrease in the resonance frequency in the case of a positive phase can be explained as the result of a lower stiffening contribution (or group effect) from the phased adjacent foundation. On the other hand, the foundation that sustains a delayed harmonic load must deal with the residual energy from the preceding adjacent foundation, hence, the higher resonance frequency.

This trend continues in cases with larger separation distances between foundations, as shown in Fig. 24 for d/b values of 4 and 6. The

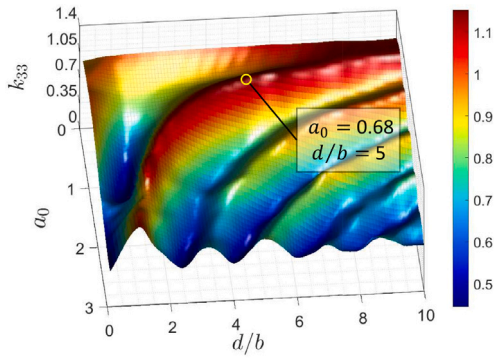

(a) k_{33} vs. a_0 vs. d/b for $\phi = -90°$.

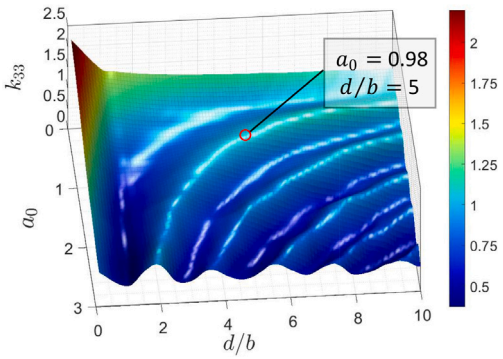

(b) k_{33} vs. a_0 vs. d/b for $\phi = -180°$.

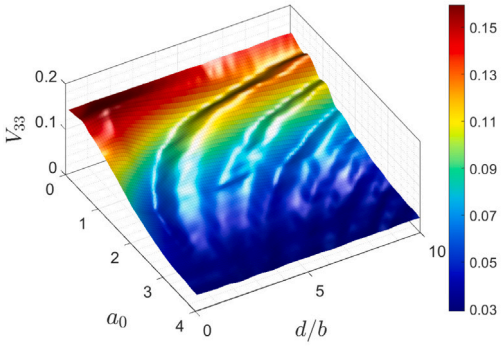

(c) V_{33} vs. a_0 vs. d/b for $\phi = -90°$.

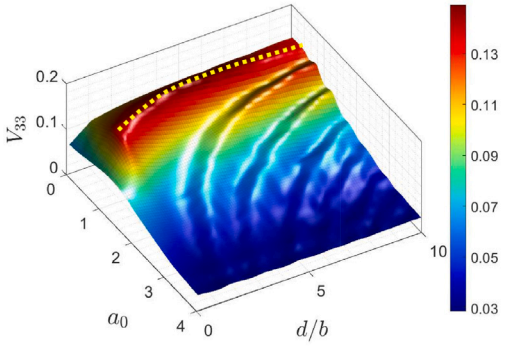

(d) V_{33} vs. a_0 vs. d/b for $\phi = -180°$.

Fig. 22. Influence of d/b on impedance and compliance surfaces for $\phi = -90°$ and $-180°$ ($\nu = 1/3$, $l/b = 1$, $\beta = 0\%$).

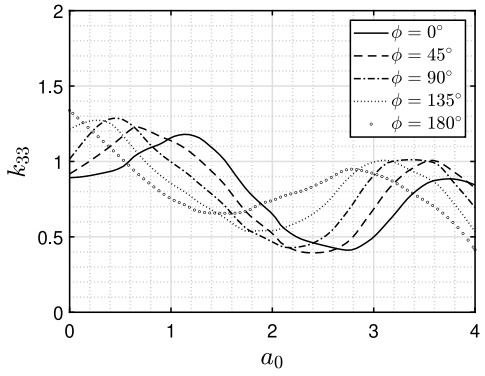

(a) k_{33} vs. a_0.

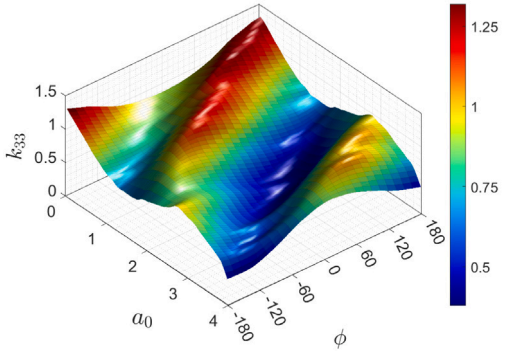

(b) k_{33} vs. a_0 vs. ϕ.

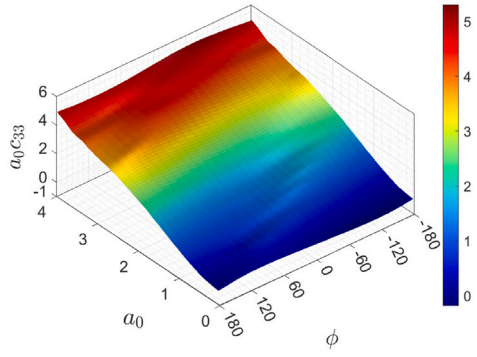

(c) $a_0 c_{33}$ vs. a_0 vs. ϕ.

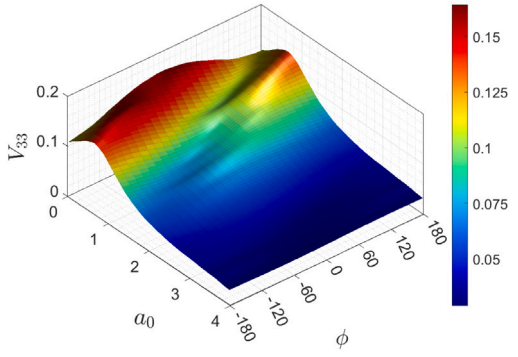

(d) V_{33} vs. a_0 vs. ϕ.

Fig. 23. Influence of phase ϕ on impedance and compliance function and surfaces ($d/b = 2$, $\nu = 1/3$, $l/b = 1$, $\beta = 0\%$).

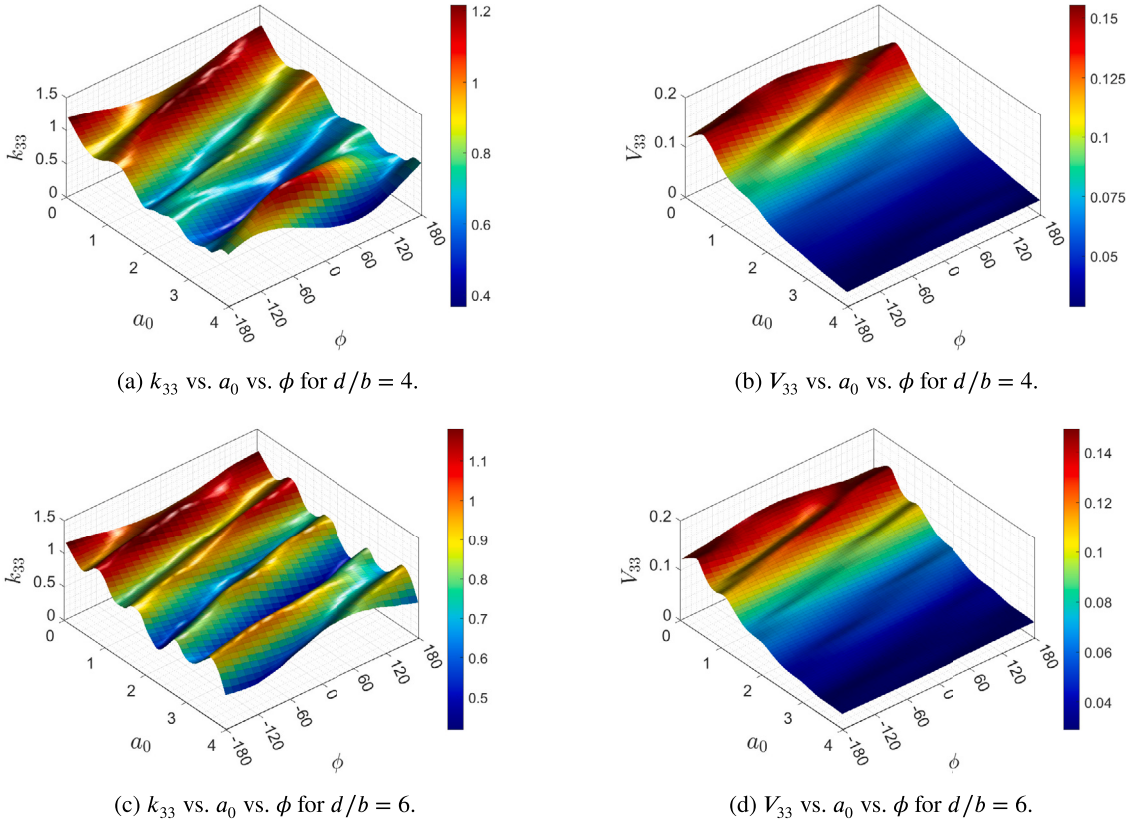

(a) k_{33} vs. a_0 vs. ϕ for $d/b = 4$.

(b) V_{33} vs. a_0 vs. ϕ for $d/b = 4$.

(c) k_{33} vs. a_0 vs. ϕ for $d/b = 6$.

(d) V_{33} vs. a_0 vs. ϕ for $d/b = 6$.

Fig. 24. Influence of phase ϕ on impedance and compliance surfaces for $d/b = 4$ and $d/b = 6$ ($\nu = 1/3$, $l/b = 1$, $\beta = 0\%$).

figure also shows the increasing number of peaks in the foundation's response in relation to the results in Fig. 9. The values of $\Delta a_0/\Delta\phi$ for $d/b = 4$ and $d/b = 6$ vary across the surface plots and tend to be higher relative to the ones for $d/b = 2$, which illustrates the nonlinear effect of interaction between the foundations' arrangement and the phase between the harmonic loads.

Fig. 25 presents the results from models with $d/b = 4$ and 6 and $l/b = 2$ and 3. The general patterns found in compliance surfaces for $l/b = 1$ (Figs. 24(b) and 24(d)) remain present. The plots in Fig. 25 also show that the phase occurring between harmonic loads influences the impedance coefficients' amplitudes in addition to the shift in the critical frequencies.

The system's kinematics can be examined as before through the phase difference between different parts of the system. Fig. 26 illustrates the kinematics of twin foundations under asynchronous loads for cases with phases between harmonic loads, ϕ, of 45°, 90°, and 180° and with $d/b = 6$, $l/b = 2$, $\nu = 1/3$, and $\beta = 0\%$. The displacement fields obtained from a model with $\phi = 45°$ show that a phase contrast of 180° can still be observed at a resonance frequency. In the case of a model with $\phi = 90°$, a 165° phase difference is observed between the response of the soil region between foundations and the reference foundation. A 180° phase contrast is no longer present.

The displacement fields obtained from a model with $\phi = 180°$ at its second resonance frequency ($a_0 \approx 1.131$) show a more complex response where, in addition to the 180° phase difference between the foundations' responses, two soil parts are formed between foundations, oscillating at a phase difference of 180° relative to each other, but not to either of the foundations. This suggests that the higher resonance frequency, in this case, is required such that the two oscillating soil parts can be formed, and the forms are oscillating at a sufficient phase following the distance required for the corresponding wavelength to transmit their inertia back to the foundations.

5. Computational aspect

One of the advantages of our hybrid BEM-FEM implementation is the ability to reuse the macro-elements or substructures for other FE models (see Fig. 4). A complete computation of a hybrid BE-FE model includes the following steps: (1) computation of the system of equations of a BE model followed by a condensation and conversion of the equations into a suitable form for the FE environment, (2) generation of a macro-element from the BE model's matrices using the substructure procedure, (3) computation of the FE model followed by the assembly of the system of equations from both subdomains into a global one, and (4) solving the system of equations using a steady-state-direct solver (see Fig. 4). Further details can be found in [30]. A partial computation using a previously generated macro-element omits steps (1) and (2), reducing the CPU time.

For the current study, a complete computation of a model with a certain angular frequency requires the following CPU times for steps (1), (2), and *(3* and *4)*: 1150 s, 200 s, and 1700 s. We performed 5794 simulations, among which 110 simulations were performed as complete computations. The rest were solved by reusing the generated substructures or macro-elements. Thus, approximately 7.7E+6 s of CPU time can be reduced, corresponding to 50.10% of the overall CPU time. When measured as the elapsed time, the computations took effectively 163 h as opposed to 817 h. This corresponds to 79,97% reduction. Additionally, data storage of approximately 7.8 terabytes can be avoided. This benefit made it possible for us to carry out the extensive numerical simulations required for the current study within a reasonable time frame.

6. Conclusions

This paper presents the results of a numerical study concerning the response of twin adjacent rigid massless surface foundations resting

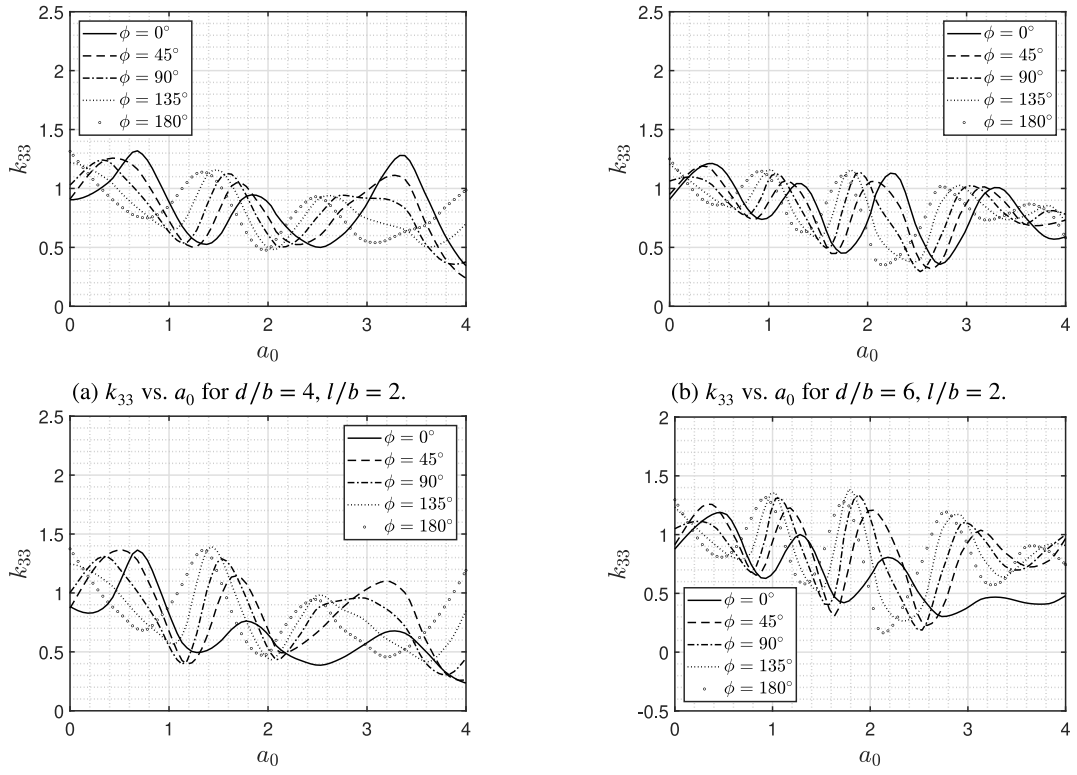

(a) k_{33} vs. a_0 for $d/b = 4$, $l/b = 2$.

(b) k_{33} vs. a_0 for $d/b = 6$, $l/b = 2$.

(c) k_{33} vs. a_0 for $d/b = 4$, $l/b = 3$.

(d) k_{33} vs. a_0 for $d/b = 6$, $l/b = 3$.

Fig. 25. Influence of phase ϕ on the real parts of impedances for $d/b = 4$ and 6 and $l/b = 2$ and 3 ($\nu = 1/3$, $\beta = 0\%$).

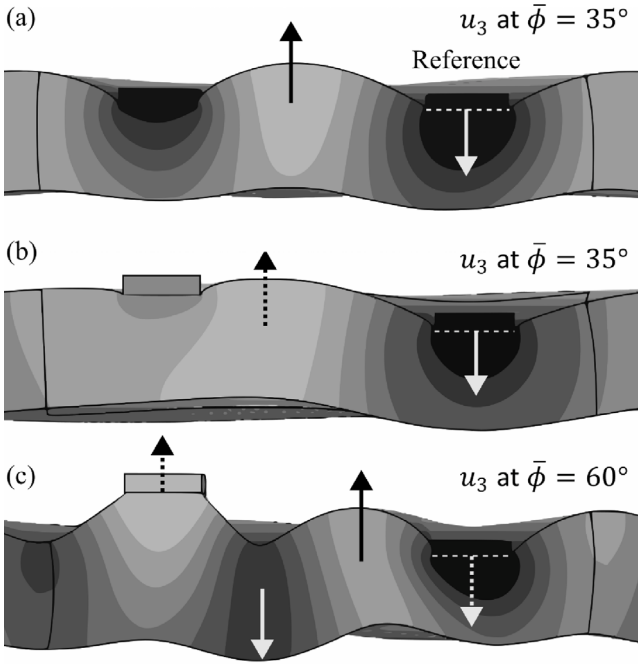

Fig. 26. Displacement pattern of twin surface foundations under asynchronous harmonic loads during resonance states: Results from model with $d/b = 6$ showing u_3 at output phases, $\bar{\phi}$, corresponding to the reference foundation's minimum vertical displacement in cases with (a) $\phi = 45°$ ($\bar{\phi} = 35°$), (b) $\phi = 90°$ ($\bar{\phi} = 35°$), and (c) $\phi = 180°$ ($\bar{\phi} = 60°$). Other parameters are $l/b = 2$, $\nu = 1/3$, and $\beta = 0\%$.

on a homogeneous half-space under synchronous and asynchronous harmonic loads. The current study is a step to better understand such a system's behavior and to provide a library of pre-calculated impedance and compliance functions for practical engineering purposes. The impedance and compliance values are presented here as 3D surfaces for completeness and to facilitate a more thorough examination of the parameters' influence. The parametric study is performed using the hybrid BEM-FEM implemented in ABAQUS and MATLAB [21,30,39].

We examine the influence of the distance between foundations, material damping, Poisson's ratio, the geometrical shape ratio of the foundations, and the phase difference between harmonic loads. Conclusions from the numerical results are summarized as follows:

- The results of the mesh convergence study show the importance of the discretization grid and mesh formulation to the simulation's accuracy. A discretization technique with a bias, e.g., as one proposed by Wong and Luco [12], is recommended to capture the stress concentration and the shorter wavelengths near the foundations' edges.
- Resonance patterns occur as a result of interaction between the foundations and soil. Increasing the foundations' distance ratio increases the number of resonance points along the same excitation frequency range. Approximation formulae are proposed to estimate the resonance frequencies as a function of the shear or Rayleigh wave velocity.
- The foundation's shape ratio tends to have an amplifying effect on the real part of impedances. However, the change in the resonance frequency is minimal. The displacement fields obtained from long rectangular foundations, i.e., approaching strip foundations, show waveforms that are inconsistent with ones of a plane strain expectation.
- The effect of soil's material damping cannot be fully decoupled in the real part of the impedances. A new relation is proposed to approximate this effect.

Table 3
List of downloadble impedance and compliance surfaces.

Prefixes	Description
Imped_k33_	Impedance surface (real part)
Imped_c33_ or Imped_a0c33_	Impedance surface (imaginary part)
Compli_V33_	Compliance surface

No.	File Name	d/b	ν	l/b	ϕ
1	DB_Surf	0–10	1/3	1	0
2	DB_Po040_Surf	0–10	0.40	1	0
3	DB_Po049_Surf	0–10	0.49	1	0
4	Po_Surf	2	1/3–0.49	1	0
5	DB2_LB_Surf	2	1/3	1–4	0
6	DB4_LB_Surf	4	1/3	1–4	0
7	DB6_LB_Surf	6	1/3	1–4	0
8	Phi_DB2_Surf	2	1/3	1	(−180)–180
9	Phi_DB4_Surf	4	1/3	1	(−180)–180
10	Phi_DB6_Surf	6	1/3	1	(−180)–180
11	Phi_DB2_LB2_Surf	2	1/3	2	(−180)–180
12	Phi_DB4_LB2_Surf	4	1/3	2	(−180)–180
13	Phi_DB6_LB2_Surf	6	1/3	2	(−180)–180
14	Phi_DB2_LB3_Surf	2	1/3	3	(−180)–180
15	Phi_DB4_LB3_Surf	4	1/3	3	(−180)–180
16	Phi_DB6_LB3_Surf	6	1/3	3	(−180)–180

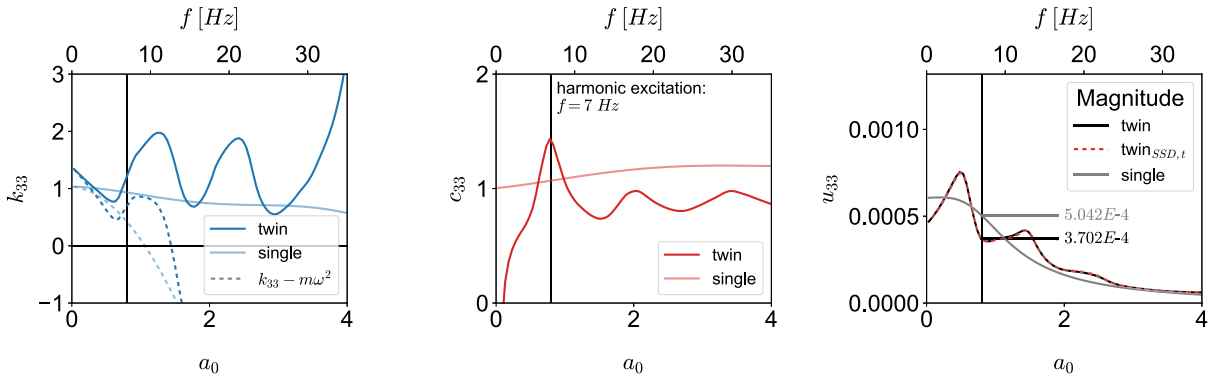

(a) k_{33} vs. a_0 for $d/b = 4$, $l/b = 2$. (b) c_{33} vs. a_0 for $d/b = 4$, $l/b = 2$. (c) u_{33} vs. a_0 for $d/b = 4$, $l/b = 2$.

Fig. 27. Comparison of the system response of harmonic-excited foundations concerning different impedance functions (ϕ =-90°, $\nu = 0.4$, $\beta = 2.5\%$).

- Increasing Poisson's ratio tends to decrease the foundation's displacement response due to the increasing incompressibility.
- The presence of a phase between the acting harmonic loads shifts the resonance patterns. An adjacent foundation having a positive phase shifts the resonance peaks of a reference foundation towards a lower frequency. For a certain foundation configuration, the rate of change of the resonance peaks varies across the frequencies and phases.

These results highlight the importance of FSFI in engineering design and optimization. It is demonstrated here that for a rather simple foundations setup, the mutual play between the key factors of spatial aspect, material properties, and sustained loads may result in complex behavior and resonance patterns.

CRediT authorship contribution statement

Hendrawan D.B. Aji: Writing – review & editing, Writing – original draft, Visualization, Validation, Software, Resources, Methodology, Investigation, Formal analysis, Data curation, Conceptualization. **Till Heiland:** Writing – review & editing, Visualization, Investigation, Formal analysis, Conceptualization. **Frank Wuttke:** Writing – review & editing, Supervision, Project administration, Funding acquisition. **Alexander Stark:** Supervision, Project administration, Funding acquisition. **Petia Dineva:** Writing – review & editing, Validation, Supervision, Methodology.

Declaration of competing interest

The authors declare that they have no known competing financial interests or personal relationships that could have appeared to influence the work reported in this paper.

Data availability

The results of the parametric study are compiled as 16 trios of 3D surfaces (real part and imaginary part of the impedances, and compliance coefficients) and publicly available as MATLAB interactive figures (FIG-file) and text files at https://doi.org/10.57892/100-50. The list of available figures is provided in the following Table 3. In addition, the figure showing curves fitted to the resonance patterns (Fig. 9(d)) is also made available.

Acknowledgments

The first author is grateful for the support by the Federal Ministry of Education and Research in Germany (BMBF) under research grant "GEOSTOR" with a grant number of 03F0893C.

Table 4
Calculation example.

	Variable	Value	Unit	Description
	Foundation			
	b	2	m	
	l	4	m	
	h	1	m	
	d	8	m	
(m1)	Mass (1 foundation)	117.60	ton	
	External load			
(p1)	P_3	−300	kN	Can be complex-valued
(p2)	f	7.00	Hz	
(p3)	ϕ	−90	°	The phase of the load on the adjacent foundation
	Soil properties			
	C_S	110	m s^{-1}	
	ρ	1800	kg m^{-3}	
	ν	0.40		
	β	0.025		
	μ	21.78	MPa	
(1)	ω	43.982	rad s^{-1}	
(2)	a_0	0.80		
(3)	d/b	4		
(4)	l/b	2		
(5)	A_b	32	m^2	
(6)	χ	0.5		Eq. (11)
(7)	C_L	198.41	m s^{-1}	Eq. (11)
(8)	K_{33}	477 908.22	kN m^{-1}	Eq. (9)
(9)	C_{33}	11 428.60	kg s^{-1}	Eq. (10)
	Real part coefficient			
(10)	$k_{33}(\omega)$ for $l/b = 1$	1.072		Surf. No. 2 (k33) in Table 3: a_0 in (2), d/b in (3)
(11)	Adjust. factor for $l/b = 1$	1.098		Surf. No. 6 (k33) in Table 3: a_0 in (2), $l/b = 1$
(12)	Adjust. factor for l/b in (4)	1.232		Surf. No. 6 (k33) in Table 3: a_0 in (2), l/b in (4)
(13)	$k_{33}(\omega)$ adjusted for l/b in (4)	1.203		(10) × (12)/(11)
(14)	Adjust. factor for $\phi = 0°$	1.257		Surf. No. 12 (k33) in Table 3: a_0 in (2), $\phi = 0°$
(15)	Adjust. factor for ϕ in (p3)	1.210		Surf. No. 12 (k33) in Table 3: a_0 in (2), ϕ in (p3)
(16)	$k_{33}(\omega)$ adjusted for ϕ in (p3)	1.158		(13) × (15)/(14)
	Imaginary part coefficient			
(17)	$c_{33}(\omega)$ for $l/b = 1$	0.831		Surf. No. 2 (c33) in Table 3: a_0 in (2), d/b in (3)
(18)	Adjust. factor for $l/b = 1$	0.863		Surf. No. 6 (c33) in Table 3: a_0 in (2), $l/b = 1$
(19)	Adjust. factor for l/b in (4)	0.915		Surf. No. 6 (c33) in Table 3: a_0 in (2), l/b in (4)
(20)	$c_{33}(\omega)$ adjusted for l/b in (4)	0.881		(17) × (19)/(18)
(21)	Adjust. factor for $\phi = 0°$	0.694		Surf. No. 12 (c33) in Table 3: a_0 in (2), $\phi = 0°$
(22)	Adjust. factor for ϕ in (p3)	1.130		Surf. No. 12 (c33) in Table 3: a_0 in (2), ϕ in (p3)
(23)	$c_{33}(\omega)$ adjusted for ϕ in (p3)	1.434		(20) × (22)/(21)
(24)	Real part	555 349.57	kN m^{-1}	$K_{33}k_{33}(\omega)$; (8) × (16)
(25)	Damped real part	532 075.12	kN m^{-1}	(24)/(1 + 2βa_0)
(26)	Imaginary part	16 389.10	kg s^{-1}	$C_{33}c_{33}(\omega)$; (9) × (23)
(27)	Damped imaginary part	17 018.16	kg s^{-1}	(26)+2β(24)/ω
(28)	$S_{33}(\omega)$	532075.12 + 748497.84i	kN m^{-1}	Eq. (21)
(29)	$S_{33}(\omega)$ (including mass)	304584.69 + 748497.84i	kN m^{-1}	(28) - (m1)ω^2
(30)	$\lvert u_3 \rvert$	3.70E−04	m	Eq. (1); | (p1)/(29)|
(31)	$\lvert v_3 \rvert$	1.64E−02	m s^{-1}	(30) × ω
(32)	$\lvert a_3 \rvert$	0.72	m s^{-2}	(30) × ω^2

Appendix. Calculation example — harmonically excited foundations

Two machines are placed on two adjacent foundations, each with dimensions of $2b = 4$ m, $2l = 8$ m, and $h = 1$ m. The foundations are separated by an 8 m clear distance, which corresponds to a center-to-center distance of 12 m. Each foundation supports a mass of 117.6 tonnes, including its own weight. The soil properties are $C_S = 110$ m s^{-1}, $\rho = 1800$ kg m^{-3}, $\nu = 0.40$, $\mu = 21.78$ MPa, and $\beta = 2.5$ %,

Each machine is designed for an operating frequency of 7 Hz. Each foundation is expected to transfer a load with a magnitude of 300 kN to the underlying soil. The machines are operated such that one machine sustains a delay of 0.1072 s relative to the other. This corresponds to a phase shift of 270°, i.e., $\phi = 360° \times \Delta t \times f$, where f is the excitation frequency.

The calculation using the provided impedances is given in Table 4, where conversion to adjust the values from $\nu = 1/3$ to 0.40 is demonstrated. The displacement magnitudes, $|u_3|$, for the upstream foundation calculated using the 3D surfaces and obtained using the hybrid numerical method are 3.70E−04 m and 3.73E−04 m, respectively. The corresponding results for the downstream one are 6.12E−04 m and 5.95E−04 m, respectively. The velocity and acceleration magnitudes of the upstream foundation calculated in Table 4 are 0.0163 m s^{-1} and 0.718 m s^{-2}, respectively, while those obtained using the hybrid method are 0.0164 m s^{-1} and 0.722 m s^{-2}, respectively.

The comparison of the displacement magnitudes calculated using impedance functions of a single foundation and the presented 3D surfaces of twin foundations reveals significant discrepancies. The displacement magnitude obtained using impedance functions of a single foundation is 5.042E−04 m (see Fig. 27). The shown discrepancy of ≈ 36 % emphasizes the relevance of the FSFI for the practical design of adjacent parallel harmonically excited foundations. Using the provided impedance functions, the natural frequencies of the system can be identified as well, as pictured in Fig. 27(c). In addition to the magnitudes of the complex calculation (see Table 4), the steady-state solution of u_{33} is calculated in the time domain as a comparative analysis. This involves subjecting the foundation to a harmonic excitation $f_h(a_0)$ and analyzing

the steady-state response of the system. The result is shown as twin$_{SSD,t}$ in Fig. 27(c). It is seen that the presented approach, together with the normalization given by Eqs. (5) and (6), is applicable in both the time and frequency domain. Material damping is taken into account using the Dobry and Gazetas' approach [44,45].

References

[1] Wolf JP. Dynamic soil-structure interaction. Prentice-hall international series in civil engineering and engineering mechanics, Prentice Hall; 1985.

[2] Kramer SL. Geotechnical earthquake engineering. Prentice-hall international series in civil engineering and engineering mechanics, Prentice Hall; 1996.

[3] Kausel E. Early history of soil–structure interaction. Soil Dyn Earthq Eng 2010;30(9):822–32. http://dx.doi.org/10.1016/j.soildyn.2009.11.001, Special Issue in honour of Prof. Anestis Veletsos.

[4] Savidis S, Richter T. Dynamic interaction of rigid foundations. In: Proc. IX. lnt. conf. SMFE. 1977, p. 36–74.

[5] Gaul L. Zur Dynamik der Wechselwirkung von Strukturen mit dem Baugrund [Ph.D. thesis], Institut für Mechanik der Universität Hannover; 1980.

[6] Triantafyllidis T, Prange B. Dynamic subsoil-coupling between rigid rectangular foundations. Soil Dyn Earthq Eng 1987;6(3):164–79. http://dx.doi.org/10.1016/0267-7261(87)90013-3.

[7] Liou G-S. Dynamic stiffness matrices for two circular foundations. Earthq Eng Struct Dyn 1994;23(2):193–210. http://dx.doi.org/10.1002/eqe.4290230207.

[8] Aldaikh H, Alexander NA, Ibraim E, Knappett JA. Evaluation of rocking and coupling rotational linear stiffness coefficients of adjacent foundations. Int J Geomech 2018;18(1):04017131. http://dx.doi.org/10.1061/(ASCE)GM.1943-5622.0001041.

[9] Kausel E, Waas G, Roësset JM. Dynamic analysis of footings on layered media. J Eng Mech Div 1975;101(5):679–93. http://dx.doi.org/10.1061/JMCEA3.0002059.

[10] Gonzales J. Dynamic interaction between adjacent foundations. Report, Massachusetts Institute of Technology; 1977, R77-30.

[11] Lin H-T, Roesset JM, Tassoulas JL. Dynamic interaction between adjacent foundations. Earthq Eng Struct Dyn 1987;15(3):323–43. http://dx.doi.org/10.1002/eqe.4290150304.

[12] Wong H, Luco J. Dynamic interaction between rigid foundations in a layered half-space. Soil Dynam Earthq Eng 1986;5(3):149–58. http://dx.doi.org/10.1016/0267-7261(86)90018-7.

[13] Qian J, Beskos DE. Dynamic interaction between 3-D rigid surface foundations and comparison with the ATC-3 provisions. Earthq Eng Struct Dyn 1995;24(3):419–37. http://dx.doi.org/10.1002/eqe.4290240309.

[14] Qian J, Beskos D. Harmonic wave response of two 3-D rigid surface foundations. Soil Dyn Earthq Eng 1996;15(2):95–110. http://dx.doi.org/10.1016/0267-7261(95)00026-7.

[15] Qian J, Tham LG, Cheung YK. Dynamic cross-interaction between flexible surface footings by combined BEM and FEM. Earthq Eng Struct Dyn 1996;25(5):509–26. http://dx.doi.org/10.1002/(SICI)1096-9845(199605)25:5<509::AID-EQE567>3.0.CO;2-Z.

[16] Betti R. Effects of the dynamic cross-interaction in the seismic analysis of multiple embedded foundations. Earthq Eng Struct Dyn 1997;26(10):1005–19. http://dx.doi.org/10.1002/(SICI)1096-9845(199710)26:10<1005::AID-EQE690>3.0.CO;2-E.

[17] Karabalis D, Mohammadi M. 3-D dynamic foundation-soil-foundation interaction on layered soil. Soil Dynam Earthq Eng 1998;17:139–52. http://dx.doi.org/10.1016/S0267-7261(97)00047-X.

[18] Sbartai B. Dynamic interaction of two adjacent foundations embedded in a viscoelastic soil. Int J Struct Stab Dyn 2016;16(03):1450110. http://dx.doi.org/10.1142/S0219455414501107.

[19] Kausel E, Peek R. Dynamic loads in the interior of a layered stratum: An explicit solution. Bull Seismol Soc Am 1982;72(5):1459–81. http://dx.doi.org/10.1785/BSSA0720051459.

[20] Kausel E. Thin-layer method: Formulation in the time domain. Internat J Numer Methods Engrg 1994;37(6):927–41. http://dx.doi.org/10.1002/nme.1620370604.

[21] Aji H, Wuttke F, Dineva P. 3D hybrid model of foundation-soil-foundation dynamic interaction. ZAMM Z Angew Math Mech 2021;101(11). http://dx.doi.org/10.1002/zamm.202000351.

[22] Zeolla E, de Silva F, Sica S. A simplified approach to account for through-soil interaction between two adjacent shallow foundations. Bull Earthq Eng 2023;21:2503–32. http://dx.doi.org/10.1007/s10518-023-01621-1.

[23] Heiland T, Aji H, Wuttke F, Stempniewski L, Stark A. Influence of soil-structure interaction on the dynamic characteristics of railroad frame bridges. Soil Dynam Earthq Eng 2023;167. http://dx.doi.org/10.1016/j.soildyn.2023.107800.

[24] Heiland T, Stempniewski L, Stark A. The dynamic characteristics of railway portal frame bridges: A comparison between measurements and calculations. Appl Sci 2024;14(4). http://dx.doi.org/10.3390/app14041493.

[25] Maritime F, Agency H. Minimum requirements concerning the constructive design of offshore structures within the Exclusive Econoc Zone (EEZ). Standard Design BSH No 7005, Federal Maritime and Hydrographic Agency (BSH); 2015.

[26] Bard P-Y, Chazelas JL, Guéguen P, Kham M, Semblat JF. Site-City Interaction. In: Assessing and managing earthquake risk. Springer Netherlands; 2006.

[27] Hwang Y-W, Dashti S, Ramirez J, Liel A, Kirkwood P, Camata G, et al. Seismic interaction of adjacent structures on liquefiable soils: Insight from centrifuge and numerical modeling. J Geotech Geoenviron Eng 2021;147:04021063. http://dx.doi.org/10.1061/(ASCE)GT.1943-5606.0002546.

[28] Kato B, Wang G. Regional seismic responses of shallow basins incorporating site-city interaction analyses on high-rise building clusters. Earthq Eng Struct Dyn 2021;50:214–36. http://dx.doi.org/10.1002/eqe.3363.

[29] Kato B, Wang G. Seismic site–city interaction analysis of super-tall buildings surrounding an underground station: a case study in Hong Kong. Bull Earthq Eng 2022;20:1–24. http://dx.doi.org/10.1007/s10518-021-01295-7.

[30] Aji H, Wuttke F, Dineva P. 3D structure-soil-structure interaction in an arbitrary layered half-space. Soil Dynam Earthq Eng 2022;159. http://dx.doi.org/10.1016/j.soildyn.2022.107352.

[31] Vicencio F, Alexander NA, Saavedra Flores EI. A State-of-the-Art review on Structure-Soil-Structure interaction (SSSI) and Site-City interactions (SCI). Structures 2023;56:105002. http://dx.doi.org/10.1016/j.istruc.2023.105002.

[32] Sextos AG, Kappos AJ. Evaluation of seismic response of bridges under asynchronous excitation and comparisons with Eurocode 8-2 provisions. Bull Earthq Eng 2009;7(2):519–45. http://dx.doi.org/10.1007/s10518-008-9090-5.

[33] Papadopoulos SP, Sextos AG. Anti-symmetric mode excitation and seismic response of base-isolated bridges under asynchronous input motion. Soil Dyn Earthq Eng 2018;113:148–61. http://dx.doi.org/10.1016/j.soildyn.2018.06.004.

[34] Mohammadi M, Karabalis D. 3-D soil-structure interaction analysis by BEM: comparison studies and computational aspects. Soil Dynam Earthq Eng 1990;9(2):96–108. http://dx.doi.org/10.1016/S0267-7261(97)00047-X.

[35] Vucetic M. Cyclic threshold shear strains in soils. J Geotech Eng 1994;120(12):2208–28. http://dx.doi.org/10.1061/(ASCE)0733-9410(1994)120:12(2208).

[36] Gazetas G, Dobry R, Tassoulas JL. Vertical response of arbitrarily shaped embedded foundations. J Geotech Eng 1985;111(6):750–71. http://dx.doi.org/10.1061/(ASCE)0733-9410(1985)111:6(750).

[37] Gazetas G. Formulas and charts for impedances of surface and embedded foundations. J Geotech Eng 1991;117(9):1363–81. http://dx.doi.org/10.1061/(ASCE)0733-9410(1991)117:9(1363).

[38] Nakamura N. Improved methods to transform frequency-dependent complex stiffness to time domain. Earthq Eng Struct Dyn 2006;35(8):1037–50. http://dx.doi.org/10.1002/eqe.570.

[39] Aji H. Hybrid BEM-FEM for 2D and 3D dynamic soil-structure interaction considering arbitray layered half-space and nonlinearities [Ph.D. thesis], Kiel University; 2023, http://dx.doi.org/10.13140/RG.2.2.20886.93767.

[40] Vasilev G, Parvanova S, Dineva P, Wuttke F. Soil-structure interaction using BEM–FEM coupling through ANSYS software package. Soil Dyn Earthq Eng 2015;70:104–17. http://dx.doi.org/10.1016/j.soildyn.2014.12.007.

[41] Smith M. ABAQUS/standard user's manual, version 6.14. United States: Dassault Systèmes Simulia Corp; 2014.

[42] Yang Z, Zou X. An analytical solution for the horizontal vibration behavior of a cylindrical rigid foundation in poroelastic soil layer. Earthq Eng Struct Dyn 2023;52(5):1617–28. http://dx.doi.org/10.1002/eqe.3855.

[43] Wolf JP. Foundation vibration analysis using simple physical models. Prentice-hall international series in civil engineering and engineering mechanics, Prentice Hall; 1984.

[44] Dobry R, Gazetas G. Dynamic response of arbitrarily shaped foundations. J Geotech Eng 1986;112(2):109–35. http://dx.doi.org/10.1061/(ASCE)0733-9410(1986)112:2(109).

[45] Heiland T. Dynamische charakteristik von eisenbahnrahmenbrücken: ein beitrag zur klärung von modelldiskrepanzen [Ph.D. thesis], Karlsruher Institut für Technologie (KIT); 2024, http://dx.doi.org/10.5445/IR/1000167926.